OPTIMIZATION OF ACQUISITION AND PROCESSING PARAMETERS IN SENTINEL LYMPH NODE SCINTIGRAPHY USING SPECT/CT MONTE CARLO SIMULATION

by

Ayşenur Yüksel

B.S. in Industrial Engineering, Istanbul Technical University, 2000

Submitted to the Institute of Biomedical Engineering
in partial fulfillment of the requirements
for the degree of
Master of Science
in
Biomedical Engineering

Boğaziçi University
2019

OPTIMIZATION OF ACQUISITION AND PROCESSING PARAMETERS IN SENTINEL LYMPH NODE SCINTIGRAPHY USING SPECT/CT MONTE CARLO SIMULATION

APPROVED BY:

Assoc. Prof. Dr. Albert Güveniş .....
(Thesis Advisor)

Assoc. Prof. Dr. Bora Garipcan .....

Assist. Prof. Dr. Mehmet Kocatürk .....

DATE OF APPROVAL: 17 May 2019

ACKNOWLEDGMENTS

I would like to express my sincere gratitude to my thesis advisor Assoc. Prof. Dr. Albert Güveniş for the continuous support of this study, for his patience, motivation, and immense knowledge.

I would also like to thank to my family and especially to my aunt Nazmiye Taylar for encouraging me throughout this thesis and my life in general.

ACADEMIC ETHICS AND INTEGRITY STATEMENT

I, Ayşenur Yüksel, hereby certify that I am aware of the Academic Ethics and Integrity Policy issued by the Council of Higher Education (YÖK) and I fully acknowledge all the consequences due to its violation by plagiarism or any other way.

Name :

Signature:

Date:

ABSTRACT

OPTIMIZATION OF ACQUISITION AND PROCESSING PARAMETERS IN SENTINEL LYMPH NODE SCINTIGRAPHY USING SPECT/CT MONTE CARLO SIMULATION

Although single photon emission computed tomography/computed tomography (SPECT/CT) systems have been in use to enhance the detection of sentinel lymph nodes SLNs with lymphoscintigraphy, recently no study has focused on optimization of acquisition and processing parameters of SPECT/CT imaging of SLN detection in breast cancer examinations using simulations. The purpose of this study was to carry out SLN detectability optimization with a SPECT Monte Carlo simulation for the first time. SIMIND Monte Carlo simulation program was used to model The Symbia T6; Siemens, Erlangen, Germany SPECT/CT system that was equipped with LMEGP and LEHR collimators. In order to simulate SPECT imaging of a realistic patient with breast cancer, a voxel-based anthropomorphic phantom by ZUBAL torso phantom was constructed. Image reconstructions with or without attenuation and scatter corrections were performed with CASToR software. Quality of reconstructed images was evaluated according to SLN contrast with respect to background. Reconstruction with attenuation correction was found to be the optimum reconstruction method for both collimators. SPECT imaging with LMEGP collimator yielded competitive results over LEHR collimator in terms of SLN contrast. The results of the study are in agreement with the literature. The method presented in this study will enable optimization of acquisition and processing parameters of SLN SPECT imaging such as different gamma camera(s), collimator settings, patient dimensions, and reconstruction correction methods (attenuation, scatter) in breast cancer examinations realistically, accurately and at a lower cost than physical phantom or patient studies.

Keywords: Anthropomorphic phantom, Attenuation, Breast cancer, Collimator, Monte Carlo Simulation, Scatter, Sentinel lymph node (SLN), SIMIND, SPECT/CT.

ÖZET

SENTİNEL LENF NODU SİNTİGRAFİSİNİN ÇEKİM VE İŞLEME PARAMETRELERİNİN SPECT/CT MONTE CARLO SİMÜLASYONU İLE OPTİMİZASYONU

SPECT/CT görüntüleme, meme kanseri teşhis ve tedavisi sırasında sentinel lenf nodu (SLN) haritalandırmasının iyileştirilmesi için lenfosintigrafiye destek olarak kullanılmakla birlikte literatürde bu konuya odaklı SPECT/CT çekim ve işleme parametrelerinin simülasyon ile optimizasyonu araştırmaları bulunmamaktadır. Bu çalışma, Monte Carlo simülasyonu ile SPECT görüntülemesinde SLN tespitinin optimize edilerek bu alandaki ilk çalışma olmayı amaçlamaktadır. Araştırmada LEHR ve LMEGP kolimatör kullanılan Symbia T6; Siemens, Erlangen, Germany SPECT/CT gama kamera sistemi SIMIND Monte Carlo simulasyon programı ile modellenmiş, antropomorfik fantom olan ZUBAL torso fantom kullanılarak oluşturulan meme kanserli gerçek bir hastanın SPECT görüntülemesi simüle edilmiştir. Rekonstrüksiyonlardaki attenüasyon ve/veya saçılma düzeltmeleri CASToR aracı ile yapılmış ve görüntü kalitesi gözlemlenen SLN kontrastına göre analiz edilmiştir. Çalışma sonucunda attenüasyon düzeltmesinin her iki kolimatör için en iyi yöntem olduğu saptanmış, SLN kontrast parametresine göre LMEGP kolimatörün LEHR kolimatör kadar iyi sonuçlar verebildiği değerlendirilmiştir. Ulaşılan sonuçlar literatür ile uyumludur. Bu araştırmada sunulan yöntem, meme kanserinde SLN SPECT/CT görüntülemesindeki gama kamera, kolimatör, hasta boyutları ve rekonstüksiyon düzeltme yöntemleri vb. çekim ve görüntü işleme parametrelerinin optimizasyonunun gerçekçi, doğru ve fiziksel fantom ve kilinik çalışmalara göre daha az maliyetli olarak gerçekleştirilebilmesine olanak kılacaktır.

Anahtar Sözcükler: Antropomorfik fantom, Attenüasyon, Kollimator, Meme kanseri, Monte Carlo Simülasyonu, Saçılma, Sentinel Lenf Nodu (SLN), SIMIND, SPECT/CT

TABLE OF CONTENTS

LIST OF FIGURES

LIST OF TABLES

LIST OF SYMBOLS

$\bar{b}$	mean count of $BackgroundROI$
k	scatter factor
p	significance
$\bar{s}$	mean count of $SLNROI$
$\#$	number

LIST OF ABBREVIATIONS

AC	Attenuation Correction
AT	Include Attenuation Correction
BMI	Body Mass Index
CASToR	Customizable and Advanced Software for Tomographic Reconstruction
CFOV	Collimator Field of View
CT	Computed Tomography
DEW	Dual Energy Window
FWHM	Full Width At Half Maximum
IS	Injection Site
ISs	Injection Sites
LEHR	Low-Energy High-Resolution
LEUHR	Low-Energy Ultra-High-Resolution
LMEGP	Low-to-Medium General-Purpose
MIP	Maximum Intensity Projection
MB	Activity In The phantom
ME	Medium Energy
MLEM	Maximum Likelihood Expectation Maximization
none	Reconstruction without correction
OSEM	Ordered Subset Expectation Maximization
ROI	Region Of Interest
SC	Scatter Correction
SD	Standard Deviation
SF	Scaling Factor Scatter
SIMIND	SIMIND Monte Carlo Program
SLN	Sentinel Lymph Node
SLNs	Sentinel Lymph Nodes
SPECT	Single Photon Emission Computed Tomography
TC	Technetium

vs	versus

1. INTRODUCTION

Breast cancer is the most frequent cancer and the leading cause of cancer death among women worldwide [1]. Lymphoscintigraphy identifying sentinel lymph nodes **(SLNs)** in more than 95% of breast cancer patients is a well established preoperative method for **SLN** mapping during breast cancer staging and treatment follow-up [2, 3]. For some patients a hidden **SLN** is non-visualized because of lymphatic drainage may not be predictable, injection site **(IS)** and **SLNs** are in close proximity causing the **SLNs** to be hidden by the scattered radiation of the **IS**, presence of extra-axillary **SLNs**, or **SLNs** not identified on lymphoscintigraphy because of excessive soft tissue attenuation in overweight and obese patient [4]. Single photon emission computed tomography/computed tomography (SPECT/CT) is the supplementary means to conventional planar imaging (lymphoscintigraphy) to increase the success of **SLN** localization in these cases.

The role of the lymph nodes in the development and spread of cancer is while preventing the spread of tumor cells also promoting the progression of tumor invasion from the lymphatic system to more remote sites [5]. The **SLN** is the first node to which lymphatic drainage and metastasis from the primary tumor occur [6]. When the histological status of the **SLN** is negative, the nodal basin can be predicted as tumor free and unnecessary axillary lymph node dissection is avoided, area of excision is reduced and the life quality of the patient is improved; when it is positive, further dissection of the nodal basin is indicated [5, 7]. Thus early and accurate mapping of all lymph nodes before surgery is clinically essential for the adequate prognosis, therapy, and outcome of breast cancer patients [6, 8].

With improved contrast, spatial resolution, and exact anatomical localization characteristics of SPECT/CT technique combined with lymphoscintigraphy may depict **SLNs**, that were missed on lymphoscintigraphy in up to 14% cases and enhance the visualization of **SLNs** up to 89-100% [9, 10]. On the other hand even both lym-

phoscintigraphy and SPECT/CT techniques are used together for **SLN** mapping it is reported in the literature [6] that there is still a detection failure rate for **SLNs** as 9% for these combined techniques. In addition, while **SLNs** could be detected in lymphoscintigraphy, they sometimes are not visualized in SPECT/CT images [4].

During preoperative **SLN** imaging of breast cancer both lymphoscintigraphy and SPECT/CT have some disadvantages. The **SLNs** are small and have low levels of radioactivity. Most of the radioactivity is up taken by the **IS** which causes decreased detectability of **SLN** because of the scattering of the gamma rays originating from the **ISs** and septal penetration of the collimators [11]. Especially when the **SLNs** are located close to the **ISs**, methods to eliminate or decrease the artifacts caused by **IS** are required [4].

The detection rate of the deeply located **SLNs** decreases because of the attenuation of gamma rays. A faint (small size and/or less activity uptake) **SLN** sometimes does not appear in SPECT/CT images and the detectability of **SLNs** maybe worse than lymphoscintigraphy images. Also image corrections (attenuation, scatter) might even result in image artifacts when **SLNs** are located close to the **ISs** and in some cases attenuation correction might cause an image artifact on the border of the lung and the breast [4].

There are several factors which affect the visibility of the **SLNs** such as the size and preparation of the radiopharmaceutical, injection techniques, the time interval between injection and imaging, gamma camera type and settings, collimator characteristics (resolution, sensitivity, septal penetration), patient age, body mass index (BMI) of the patient, patient displacement maneuvers, techniques for marking and outlining the body of the patient, and image processing and correction parameters [6, 7, 12, 13, 14]. In addition to these there is no standardized **SLN** procedure in the literature, and this may lead variable false-negative and **SLN** identification rates among the various studies [5]. Therefore in order to increase the detectability of **SLNs** there is a need to evaluate the optimum imaging protocols for the SPECT/CT acquisition[7].

It is reported that developing optimum methods for eliminating or reducing the artifacts caused by the **ISs** takes precedence in case of **SLNs** being located close to the **IS** [4].

Phantom studies, in general, are useful for development and improvement of existing and new imaging technologies and protocols. However the anatomic structure, variable scatter, attenuation and nonuniform activity distribution in the upper thoracic region cause very simple realistic phantoms to be insufficient for the studies focused on imaging of breast and associated axillary **SLNs** [15]. In order to offer accurate results for clinical studies realistic anthropomorphic digital phantoms maybe an alternative solution.

Using a **LEHR** collimator is the standard procedure for lymphoscintigraphy and additional SPECT/CT imaging [12]. High-resolution collimators with thinner septa such as **LEHR** collimator are subject to septal penetration and blurred image on the other hand high sensitivity collimators with thicker septa such as **LMEGP** might lead to improved image quality. Collimator selection is a trade off between resolution and sensitivity therefore in order to improve image quality, collimator optimization studies takes precedence for also SPECT/CT systems.

Lerman et al. [8] assessed the role of attenuation correction in improved detection of **SLN** by SPECT/CT for 29 overweight or obese breast cancer patients with non-visualized **SLNs** by planar imaging. They concluded that SPECT/CT with attenuation correction is attributable to better **SLN** image quality.

In their both clinical and physical phantom research Yoneyama et al. [16] investigated the choice of optimum collimators in SPECT/CT imaging system during preoperative **SLN** mapping of breast cancer. They reported that when compared with low-energy high-resolution **(LEHR)** collimator, the lower septal penetration characteristics of low-to-medium-energy general-purpose **(LMEGP)** collimator leading to decreased star-shaped artifact could compensate its lower resolution characteristics disadvantage and result in improved visualization of **SLNs** especially if they are lo-

cated close to the **ISs**. They also added that the radioactivity of the **SLN** and its distance from the **IS** affected the **SLN** contrast. According to their phantom study for an **SLN**, 3cm or 6cm away from the **IS**, the image contrast was the best for **LMEGP** collimator. The worst image contrast for both cases belonged to the **LEHR** collimator without lead shield.

Yoneyama et al. [4] in their subsequent study over a group of 55 females with diagnosed breast cancer searched the optimum image correction solution for improving the detectability of the **SLNs** with SPECT/CT imaging. Based on the findings of their previous study, they performed the SPECT/CT imaging with a **LMEGP** collimator instead of a **LEHR** collimator [16]. They concluded that in case of SPECT/CT is used attenuation correction should be performed as it improved the **SLN** detection rate. They also reported that scatter correction should not be performed, because scatter correction caused disappearance of a faint **SLN** in some cases.

Although SPECT/CT systems have been performed to enhance the detection of **SLNs** with lymphoscintigraphy there are limited studies [4, 8, 16] in the literature which focused on the optimization of the **SLN** detectability with SPECT/CT in breast cancer. However these studies are either clinical or physical phantom studies with a visual image interpretation method. Recently no study has focused on optimization of SPECT/CT systems on **SLN** detection in breast cancer examinations using a digital simulation technique.

In order to develop and evaluate especially scatter and attenuation corrections methods for image improvement, Monte Carlo methods and programs with digital phantoms are commonly utilized as important tools for analyzing the effects of nuclear imaging system parameters upon image quality [17, 18]. With an accurate model of the imaging system and a realistic model of the patient geometry and activity distribution Monte Carlo simulations can provide clinically highly realistic images and a real patient like measurements [19].

It is reported in the literature that besides their time, cost and easy to re-

peat/modify advantages over experimental (clinical, phantom) studies, Monte Carlo simulations have the capability of obtaining results that are impossible to be measured experimentally and therefore support the optimization of imaging systems [19].

In order to perform clinically realistic Monte Carlo simulations using digital anthropomorphic phantoms rather than phantoms based on simple geometries enable modeling the organs and structures in the patient body accurately and easily [20].

The purpose of this study is to simulate and optimize the **SLN** detectability in breast cancer with SPECT Monte Carlo Simulation on an anthropomorphic digital phantom.

The study is aimed to evaluate the effects of important parameters such as gamma camera type, collimator type, reconstruction methods (attenuation and scatter correction) of **SLN** imaging during breast cancer diagnosis and treatment accurately, easily, and at a lower cost than physical phantom or patient studies.

This study will be the first study carried out with Monte Carlo simulation using a digital phantom in SPECT/CT **SLN** detectability optimization.

In the **Methods** section of the article digital phantom construction, **SPECT** simulation, image reconstruction, and analysis & evaluation methods implemented in the study are defined. In the **Results** section the outcomes of the study are presented. Main findings of the study are explained in terms of underlying theory and potential errors and compared with results from literature in the **Discussion** section together with the potential clinical applications, benefits, limitations, and future work regarding the study. The purpose, lessons learned, and the importance of the study are restated in the **Conclusions** section. The report is ended with the **Appendix** and **References** sections.

2. METHODS

2.1 General Approach

In order to have a validated simulation and optimization method the main approach of this study was to realistically simulate the physical phantom and clinical studies performed by Yoneyama et al. [4, 16] so far as applicable and evaluate the findings of this study with the results reported in their studies. Missing data for the simulation was obtained from other studies in the literature.

SIMIND Monte Carlo simulation program (**SIMIND**) version 6.1 [21] was used as the Monte Carlo Program for SPECT camera simulations. In order to simulate a realistic patient **ZUBAL** phantom [22], a voxel-based human male torso anthropomorphic phantom with no arms and legs was used. The **ZUBAL** phantom is one of the most widely used digital phantoms in research and it is also supported in the Monte Carlo program **SIMIND**. In the study, an **IS** and an **SLN** were placed into the phantom by **SIMIND**.

SIMIND simulations were reconstructed with or without attenuation and scatter corrections by Customizable and Advanced Software for Tomographic Reconstruction **(CASToR)** software Version 1.0 [23] via a conversion program called **smc2castor** embedded in **SIMIND**. Image processing and analysis were performed with **ImageJ** 1.51k [24].

The Symbia T6; Siemens, Erlangen, Germany SPECT/CT system equipped with low-energy high-resolution **(LEHR)** and low-to-medium-energy general-purpose **(LMEGP)** collimators were modeled by **SIMIND**.

2.2 Digital Phantom Construction

The **ZUBAL** phantom has $128 \times 128 \times 243$ byte volume with isotropic voxel dimensions of $4mm$ and consists of a set of $8bit$ coded images where each voxel has a unique value that can be related to the organ or structure that the voxel belongs to. These coded images can then be used to define either density maps or activity maps provided that the user has appropriate density and activity values [21].

Generally an axillary **SLN** is located at the junction of the fatty breast tissue and chest wall and lateral to or within the borders of the pectoralis minor muscle [6, 25, 26] **SLN** and **IS** were located in the phantom referencing the SPECT/CT images in the studies of Yoneyama and his friends [4, 16].

Yoneyama et al. [16] used **SLNs** with varying activity concentrations and volumes of in their physical phantom study where the minimum **IS:SLN** radioactivity concentration ratio was $25 : 1$.

SIMIND enables to create activity maps from **ZUBAL** phantom with a user-written table in a ***.zub file**. In this study **simind.zub** file was used as the activity map where the name, unique code, density value ($g/cm^3 \times 1000$) and relative activity concentration (MBq/cc) of the organs were defined respectively.

Relative activities of **SLN**, **IS** and **Background** defined in the **ZUBAL** phantom have been defined in Table 2.1.

Table 2.1
Relative Activity Distribution of SLN, IS, and Background in the Zubal Phantom.

	Relative Activity (MBq/cc)
IS	250
SLN	10
Background	0

According the literature [11] most of the activity injected in the patient is retained in the **IS** therefore the relative activity concentrations of the background of the **SLN** (Background) and whole organs in the **ZUBAL** phantom were ignored and assigned to zero. The content of the **simind.zub** file is illustrated in Figure 2.1.

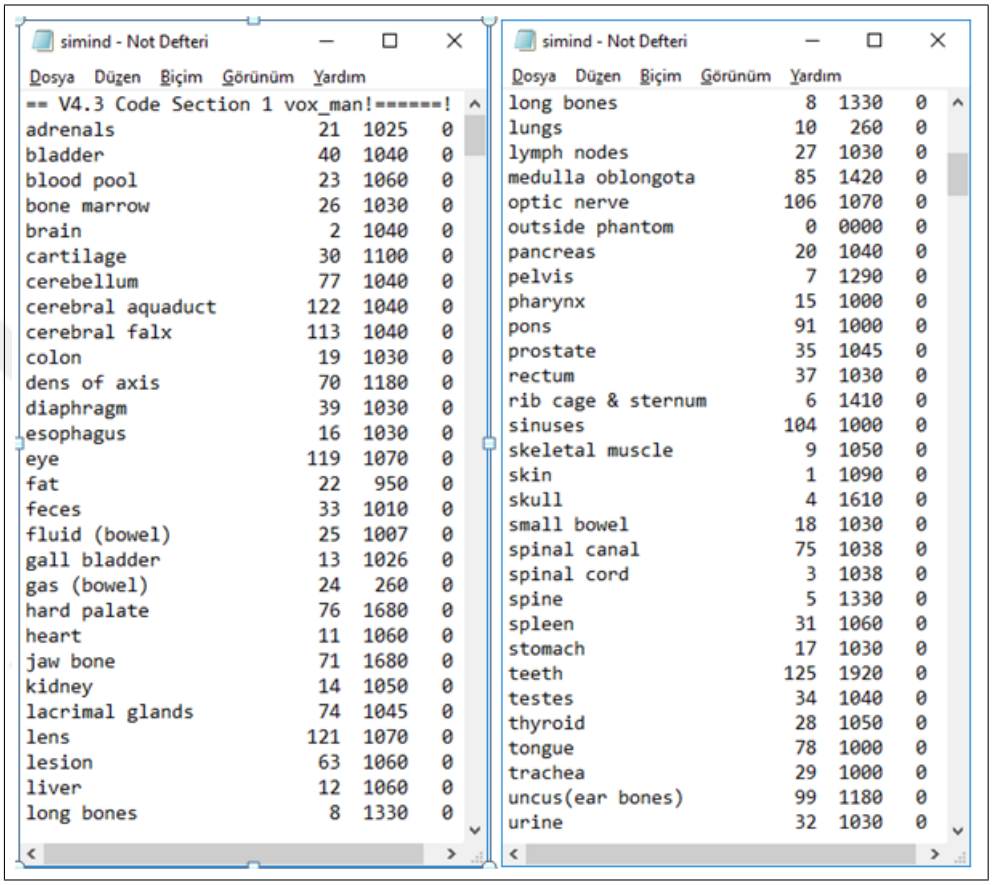

Figure 2.1 The content of simind.zub file.

An **IS** with only one axillary **SLN** was placed in digital phantom for analysis simplicity as the tumor cells initially spread through the lymphatic pathway to at least one **SLN**.

According to the voxel size ($4mm$) limitation, cylindrical **IS** and **SLN** dimensions were chosen in accordance with the physical phantom dimensions defined in the study of Yoneyama et al. [16] namely; $1.6cm$ ($4pixels$) in diameter and $0.8cm$ ($2pixel$) thick for **IS**; $0.8cm$ ($2pixel$) in diameter and $0.8cm$ ($2pixel$) thick for **SLN**. **IS** had a $32voxel$ and **SLN** has a $8voxel$ volume.

Axillary **SLN** near **IS** was located in the **ZUBAL** phantom in accordance with the SPECT/CT images given in the studies of Yoneyama et al. [4, 16]. The center-to-center distance of the axillary **SLN** to **IS** was selected as $3cm$ ($7pixels$). The distance of axillary **SLN** origin to the body surface was chosen approximately $1.5cm$ ($4pixels$). **IS** and **SLN** dimensions, x, y, z coordinates, relative activity, density, cut-off and order of inner distribution of activity data can be added to **ZUBAL** phantom with the **SIMIND *.inp** file. **IS** and **SLN** dimension and activity data given in Table 2.2 was defined and added to **ZUBAL** phantom with **simind.inp** file illustrated in Figure 2.2. A zero density means that the density is given by the original values in the voxels that the ROI occupies. Distribution of activity (cut-off and order) with a zero value indicates that there is a uniform distributed activity in the ROI [27].

Table 2.2
IS and SLN Data defined in simind.inp file.

	x radius ($pixel$)	y radius ($pixel$)	z radius ($pixel$)	x position ($pixel$)	y position ($pixel$)	z position ($pixel$)	Relative activity (MBq/cc)
IS	2	2	2	90	27	45	250
SLN	1	1	1	88	26	38	10

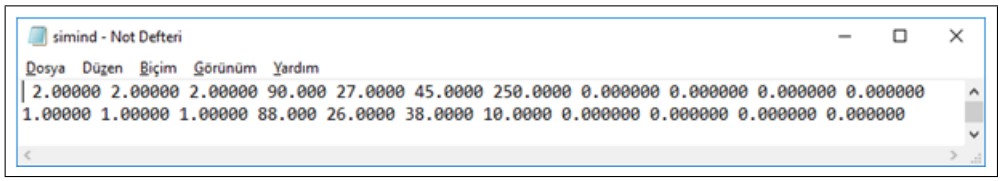

Figure 2.2 The content of simind.inp file.

A patient was assumed to have been injected a $37MBq$ ($1mCi$) dose of technetium-99m (^{99m}Tc) around the tumor in the right breast. This injection region around the tumor was called as the injection site **(IS)**. The duration between injection time and SPECT/CT imaging performed after lymphoscintigraphy was taken approximately $6hours$ (one-half life of ^{99m}Tc) according to the study reports of Yoneyama et al. [4, 16].

Symbia T6; Siemens, Erlangen, Germany [28] equipped with either **LEHR**

or **LMEGP** parallel-hole collimators was chosen as the SPECT/CT camera system. Detector and crystal parameters of **Symbia T6 SPECT/CT** system are included in Table 2.3 and Table 2.4.

Table 2.3
Detector Parameters of Symbia T6; Siemens, Erlangen, Germany.

Intrinsic Spatial Resolution FWHM in CFOV	≤3.8 mm
Intrinsic Energy Resolution FWHM in CFOV	≤9.9%

Table 2.4
Crystal Parameters of Symbia T6; Siemens, Erlangen, Germany.

Size	59.1cm ×44.5cm
Diagonal	73.9cm
Thickness	9.5mm

The **LEHR** and **LMEGP** collimator specifications represented by Yoneyama et al. and Inoue, Yusuke et al. in their studies [4, 29] were used in the study as both simulation input and evaluation method of the simulation outputs. These collimator specifications are given in Table 2.5.

While Yoneyama et al. [4, 16] implemented 60 projections in steps of 6° over 360° and performed resolution recovery in their study [4] because resolution correction was not applied during the study, SPECT images were taken with 120 equally spaced projection angles in a 360° stepwise rotation [12]. A time per view of $20s$ in a 128×128 data matrix and 15% energy window centered on $140keV$ were used.

Acquisition of simulation data was simulated for two energy windows using **SIMIND "scattwin"** scoring routine to collect counts and prepare separate images for each window. **Dual energy window (DEW)** method with energy windows namely photo-peak window ($129.5 - 150.5keV$ for ^{99m}Tc) and low-energy scatter window (92 −

Table 2.5
Specifications of LEHR and LMEGP Collimators.

	LEHR	LMEGP
Vendor	Siemens	Siemens
Septa length (mm)	24.05	37.00
Hole diameter (mm)	1.11	2.5
Septa Thickness (mm)	0.16	0.6
Sensitivity @ $10cm/collimator(cpm/kBq)$	5.5	9.2
System resolution FWHM @ $10cm(mm)$	7.4	10.4
Penetration @ $140keV(\%)$	1	<0.1
Energy at 5% septal penetration (keV)	160	240

$129.4keV$) were defined according to the tailoring of Sadrmomtaz et al. [30] report with 15% energy window applied in this study. These energy windows were included in simulation by **simind.win** file depicted in Figure 2.3. Scatter image generated for low-energy scatter window was used for scatter correction during reconstruction.

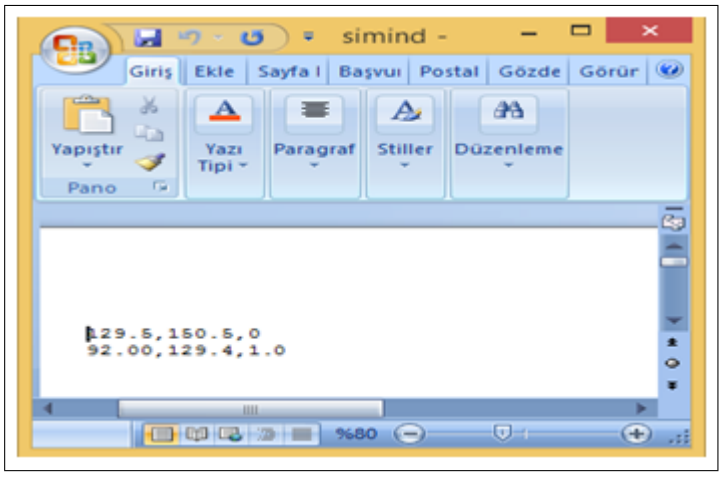

Figure 2.3 simind.win file including two energy window settings.

The coordinate system used in **SIMIND** simulation is illustrated in Figure 2.4. When simulating voxel-based phantoms, the first density/activity image is located towards $+X$ and the last one is located towards $-X$. In SPECT simulations the camera rotates in the ZY plane either clockwise or counter-clockwise [27].

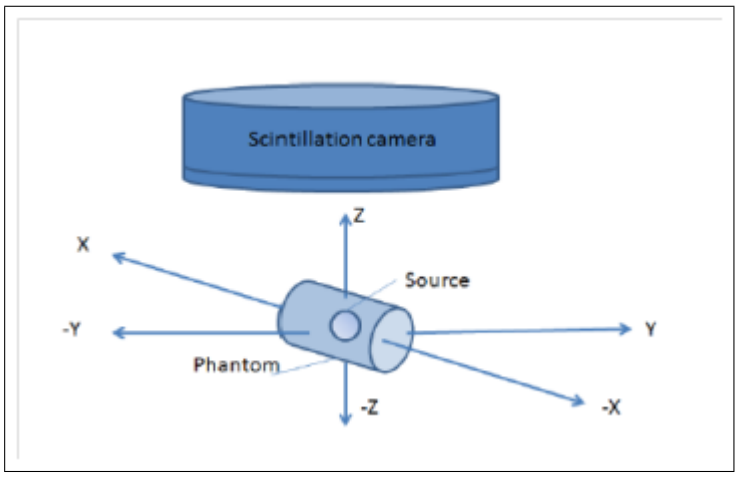

Figure 2.4 SIMIND Coordinate System.

As distance between the patient and the scintillation camera is important for image resolution and scattering of the photons, attention was given to reduce to the patient-gamma camera distance. Therefore the lowest probable distance was assigned to the **Index 12: Height to Detector Surface** parameter.

SIMIND has two main programs: **CHANGE** and **SIMIND**. The imaging system is defined in **CHANGE** program and **SIMIND** program performs the simulations and reports the simulation and reconstruction results. Simulation inputs of this study were defined in **CHANGE** program according to the **SIMIND** Manual [27] and are given through Figure 2.5-Figure 2.14.

2.3 Reconstruction

In order to obtain results with realistic noise properties, the poisson noise was added to noise-free **SIMIND** SPECT simulation data with **MosaicSuite for ImageJ and Fiji** [31] before reconstruction. **SIMIND** simulations were reconstructed with Customizable and Advanced Software for Tomographic Reconstruction (**CASToR**) software Version 1.0 [23] by a conversion program called **smc2castor** supported by **SIMIND**.

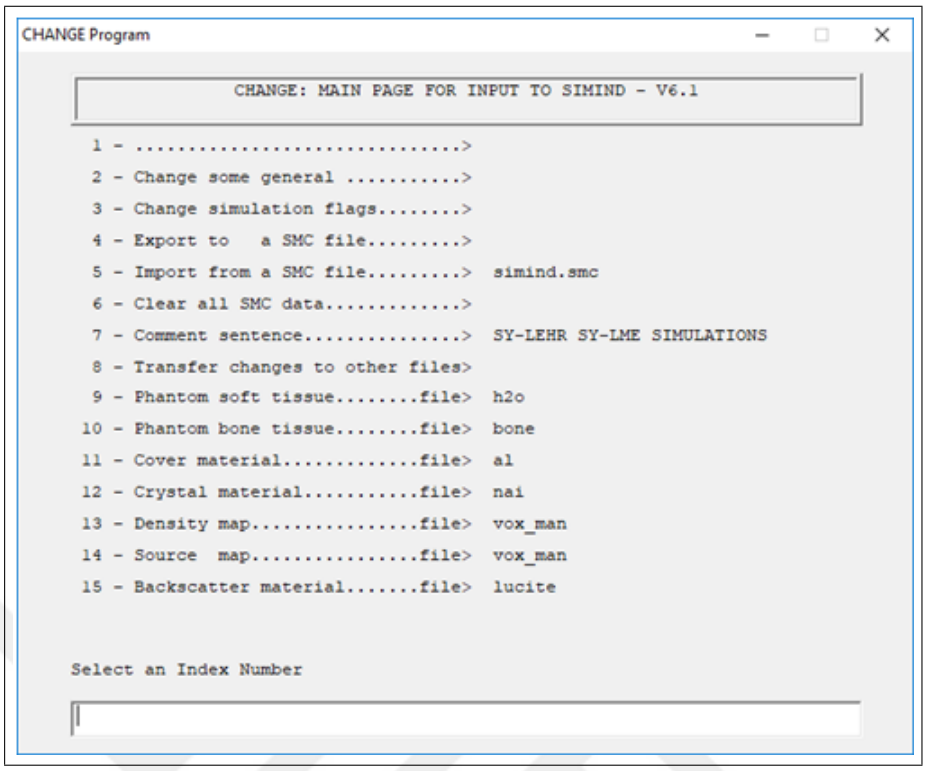

Figure 2.5 CHANGE: Main Page for Input to SIMIND - V6.1.

Dual energy window with a $k-factor(0.5)$ was chosen as the scatter correction method according to the studies [4, 30, 32, 33, 34, 35] in the literature. The scatter was estimated based on the two energy windows in **simind.win** file illustrated in Figure 2.3. Scatter correction was added to the reconstruction by assigning $k-factor(0.5)$ to the **smc2castor** program **SF: Scaling Factor Scatter** switch as "$/SF:0.5$".

Attenuation map of **SIMIND** generated simulation data was produced by setting **Flag15: Save Aligned Density Map** of **SIMIND CHANGE** program to **"TRUE"** and in order to change the data format of attenuation map the switch **in:x22, 5x** was added to the **SIMIND** simulation command line. Attenuation correction was included to the **CASToR** reconstruction with **AT: Include Attenuation Correction** switch of **smc2castor** program.

CASToR reconstructions were performed using an iterative method based on a **maximum-likelihood expectation-maximization (MLEM)** algorithm with 12 iterations and 15 subsets. In the study attenuation and scatter corrections were per-

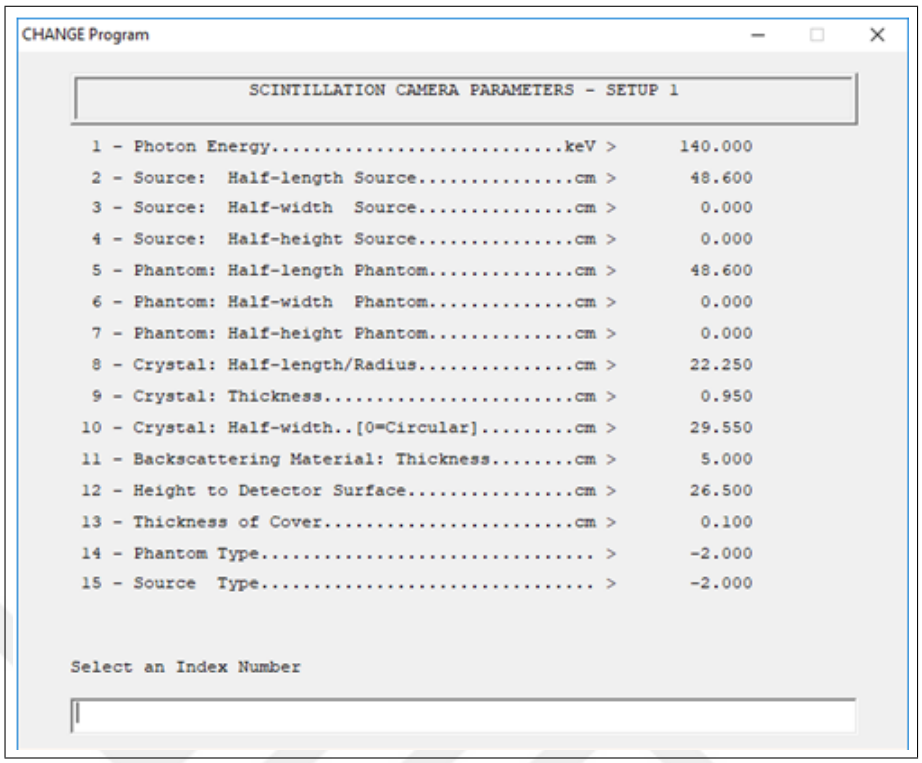

Figure 2.6 Scintillation Camera Parameters - Setup 1.

formed and the other methods such as resolution correction, pixel truncation or gaussian filter were excluded during reconstruction.

For each simulation with either **LEHR** or **LMEGP** collimators, images were reconstructed using 4 different reconstruction choices namely, **attenuation correction**, **scatter correction**, **attenuation+scatter correction** and **no correction (none)**. In order to have comparable **SLN** counts with the study results reported by Yoneyama et al. [16] the **SLN** counts of the poisson noise added simulations were tried to be normalized with **MB: Activity In The Phantom** switch of **smc2castor** program. To assign a default value to **MB** switch for each reconstruction the **SLN** count in the reconstructed image of **LMEGP** without any attenuation or scatter correction was scaled with the regarding count result of Yoneyama et al. [4].

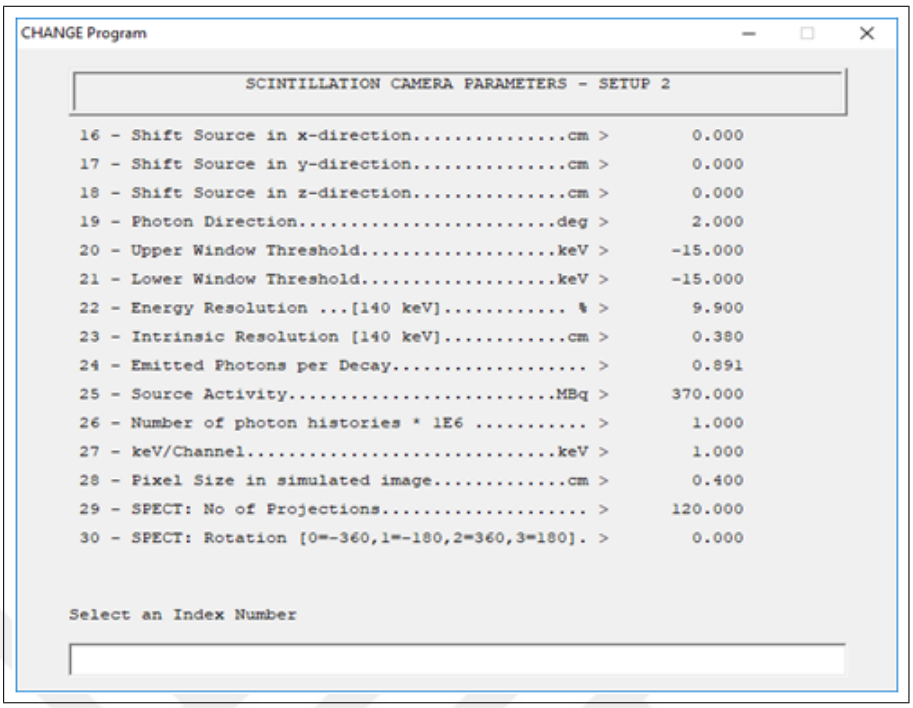

Figure 2.7 Scintillation Camera Parameters - Setup 2.

2.4 Evaluation and Statistical Analysis

The detectability of the **SLN** in reconstructed images was evaluated by the **SLN** contrast with respect to background. **ImageJ** [24] was used to analyze the images. **SLN** region of interest ($SLNROI$) was analyzed from the image slices (namely 29/60, 30/60 or 31/60) in which the mean count of the **SLN** is the highest. $SLNROI$ and background ($BackgroundROI$) were decided referencing the study of Yoneyama et al. [16]. As the coordinates and dimensions of **SLN** and **IS** were known values (Table 2.2, Figure 2.2) a $2 \times 2 pixel$ $SLNROI$ was placed at the origin of the **SLNs** $3cm$ away from the center of the **IS** in reconstructed images. $BackgroundROI$ was chosen as an area of $5 \times 5 pixel$ around the **SLN ROI** and approximately in $3cm$ from the center of the **IS**. An illustration of **SLN ROI**, **Background ROI**, and **IS** is illustrated on a reconstructed image in Figure 2.15.

SLN contrast was evaluated quantitatively according to the Eq.2.1 used in the study of Yoneyama et al. [16]:

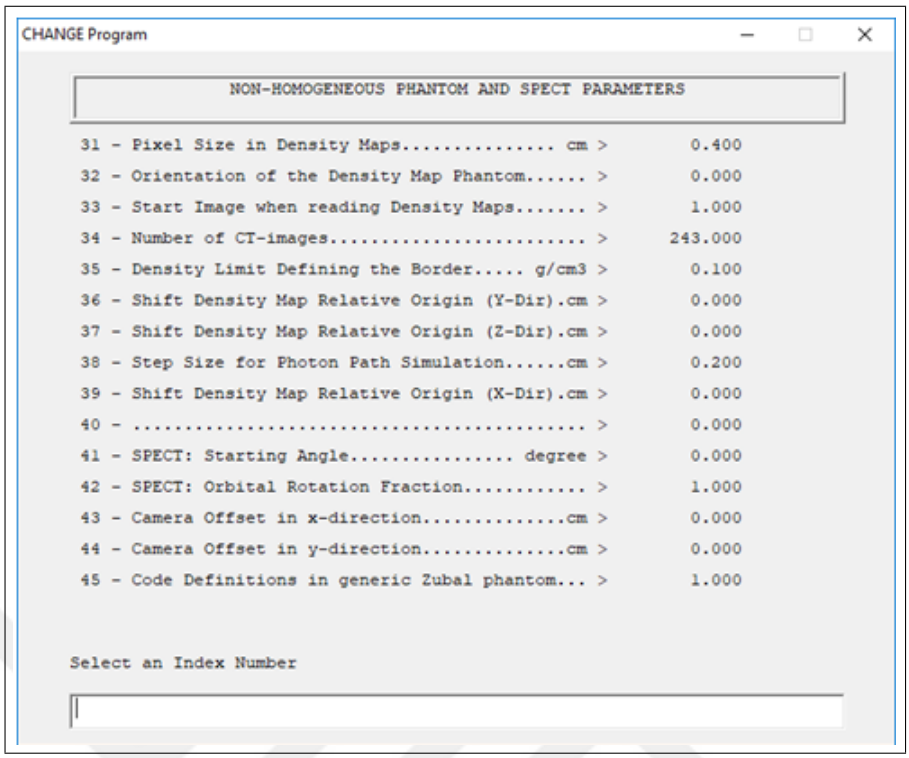

Figure 2.8 Non-homogenous Phantom and SPECT Parameters.

$$Contrast = \frac{\bar{s} - \bar{b}}{\bar{s} + \bar{b}} \tag{2.1}$$

Where; $\bar{s}$: mean count of $SLNROI$, and $\bar{b}$: mean count of $BackgroundROI$.

In order to increase the sample size and to normalize the randomness effects of the simulations, and to have more dependable results SPECT simulations were repeated for 10 times for both **LEHR** and **LMEGP** collimators resulting in a total of 20 SPECT simulations. The **SLN ROI** and **Background ROI** counts measured and the contrast values calculated for both collimators were averaged and the standard deviations were predicted accordingly. The average contrast results of the total number of 80 images projected with different collimators (**LMEGP, LEHR**) and reconstructed with different reconstruction methods were compared with each other and the results of studies of Yoneyama et al. [4, 16]. The average contrast results of the reconstruction methods were compared performing **Wilcoxon signed rank test** -a nonparametric statistical test- with a statistical significance $\alpha = 0.01$.

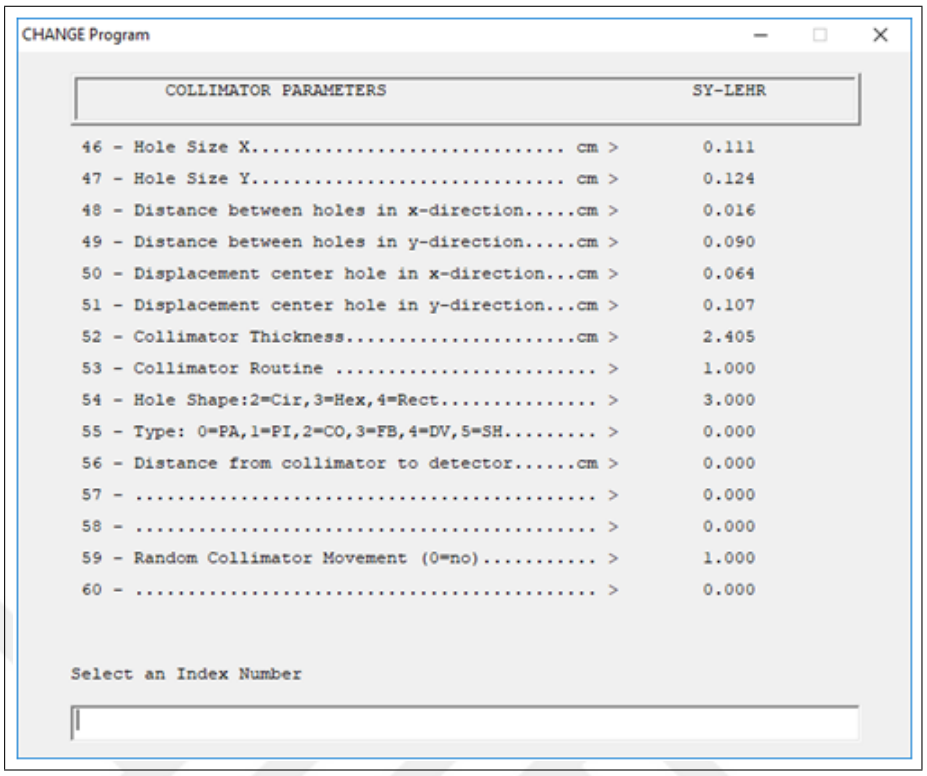

Figure 2.9 LEHR Collimator Parameters.

The effects of scatter correction (SC) and attenuation correction (AC) were evaluated using Eq.2.2 and Eq.2.3 [4].

$$Effect\ of\ SC = 100\frac{The\ counts\ decreased\ by\ SC}{The\ counts\ obtained\ without\ SC} \tag{2.2}$$

$$Effect\ of\ SC = 100\frac{The\ counts\ increased\ by\ AC}{The\ counts\ obtained\ without\ AC} \tag{2.3}$$

As an additional verification method of the study the average **Sensitivity** (cpm/kBq) **and Penetration (%) After collimator** parameters of both collimators were calculated according to the related data in **SIMIND** simulation reports. The results were compared with the literature for consistency.

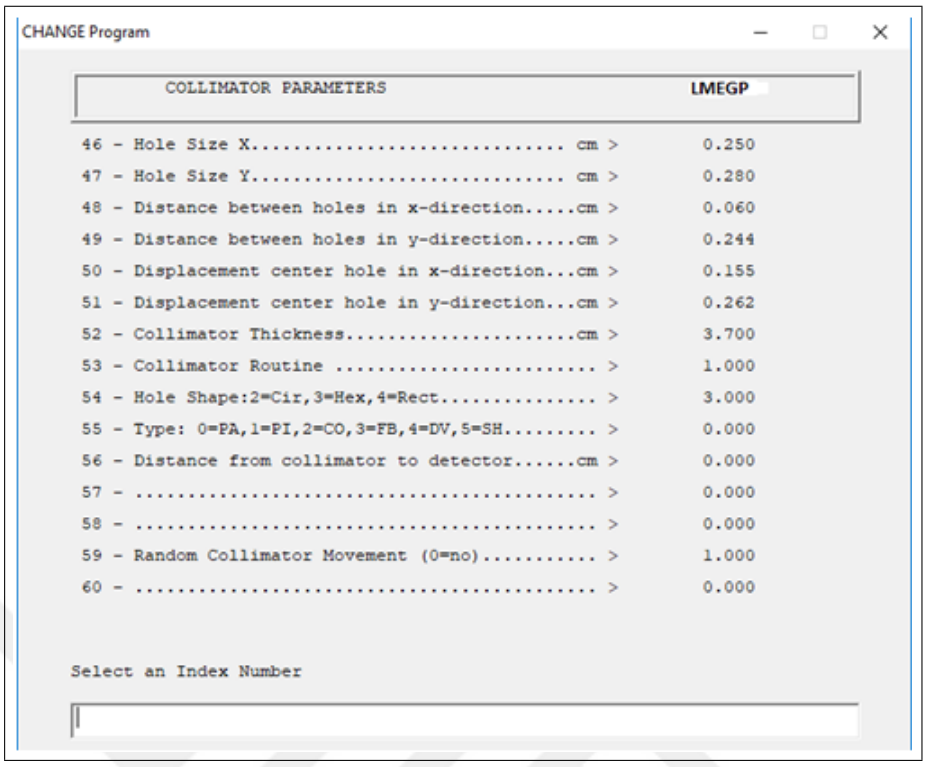

Figure 2.10 LMEGP Collimator Parameters.

Although the study was based on a quantitative analysis method, to identify the **SLNs** with a visual evaluation method Maximum Intensity Projection **(MIP)** images of the sample images were generated by **ImageJ** [24].

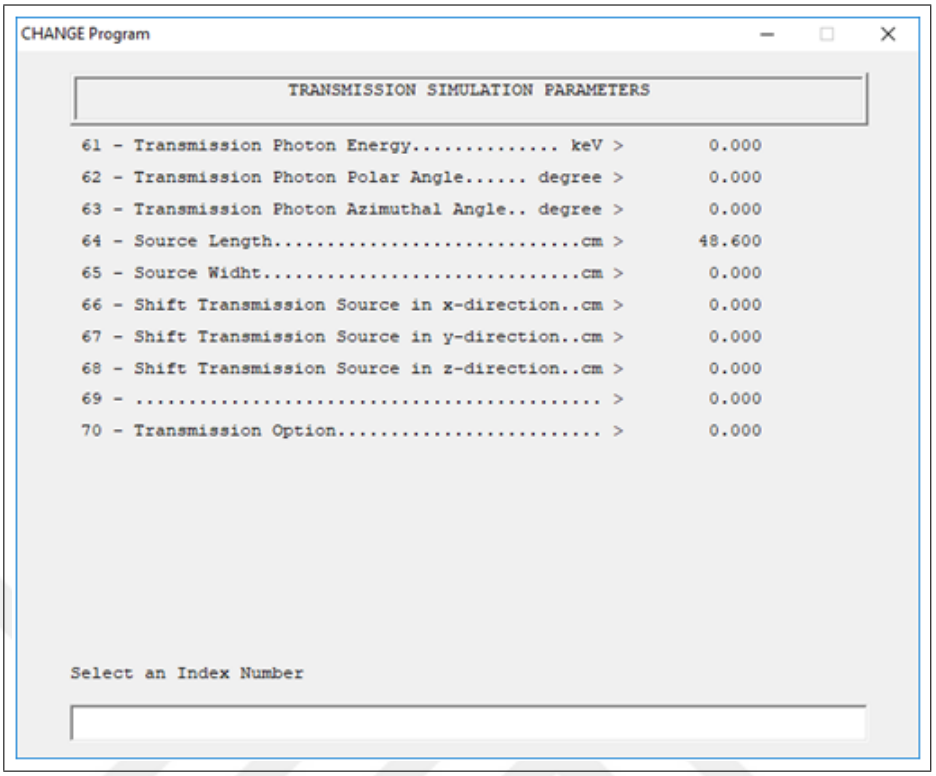

Figure 2.11 Transmission Simulation Parameters.

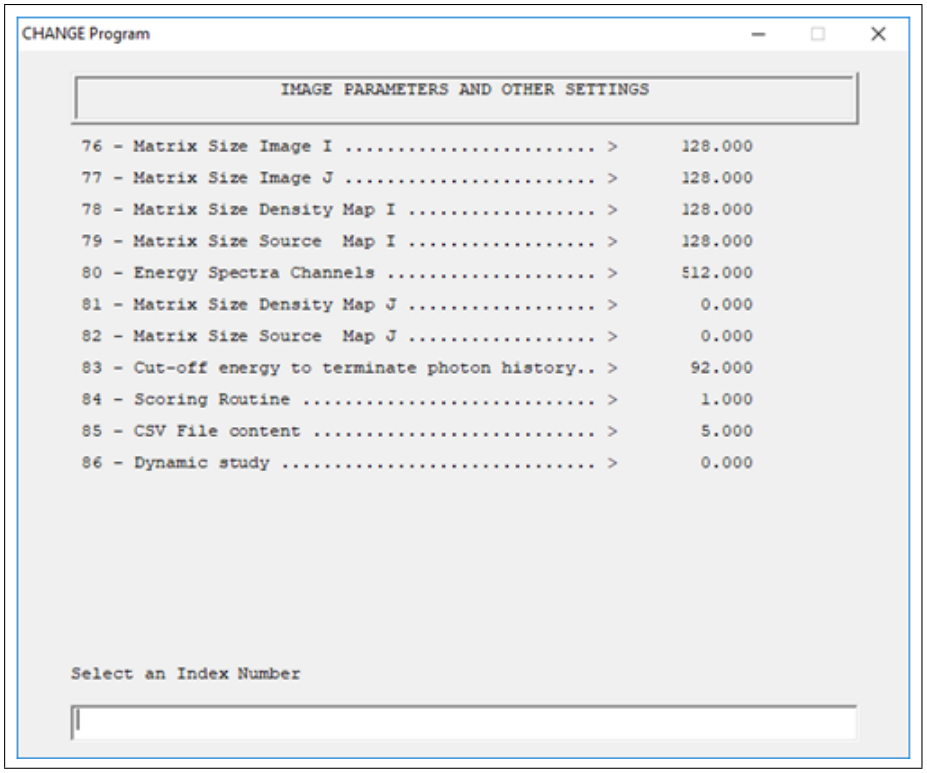

Figure 2.12 Image Parameters and Other Settings.

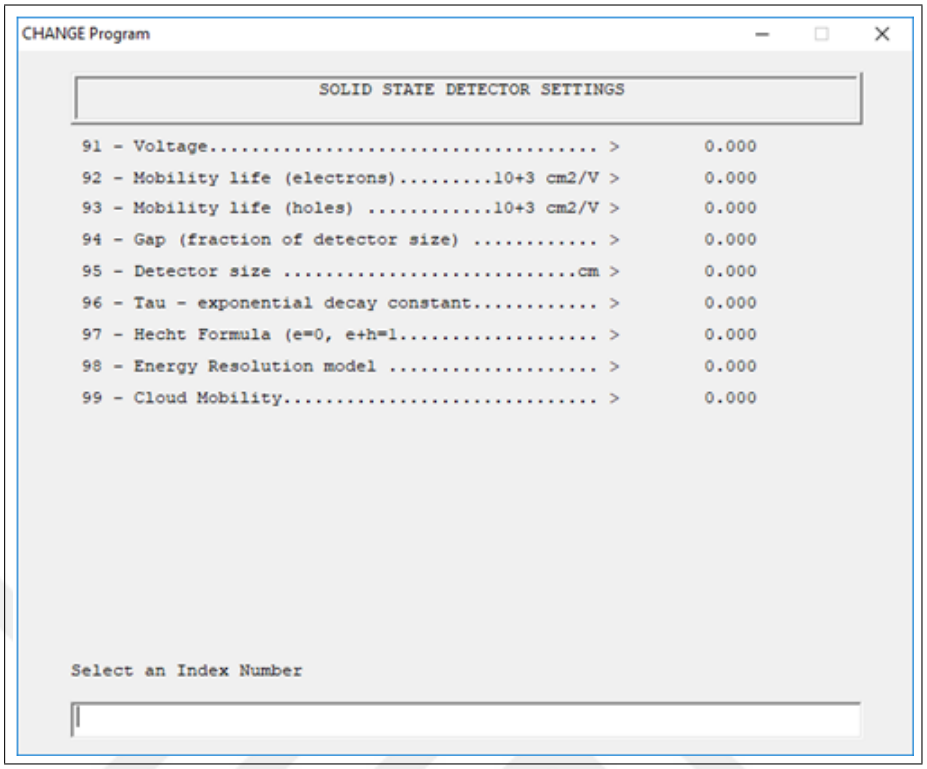

Figure 2.13 Solid State Detector Settings.

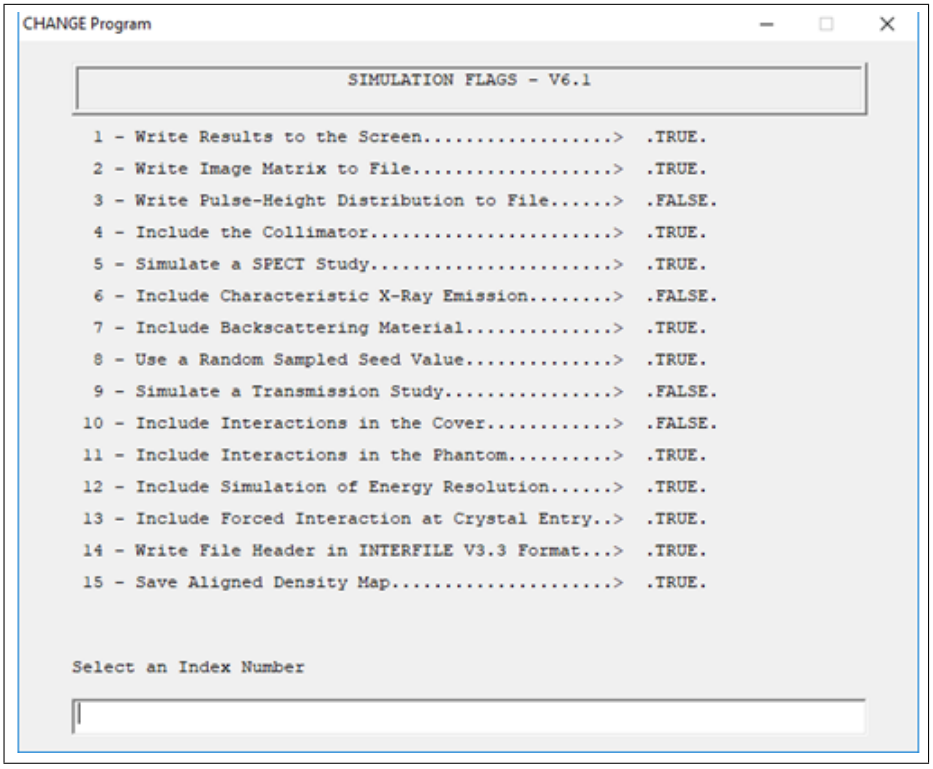

Figure 2.14 Simulation Flags.

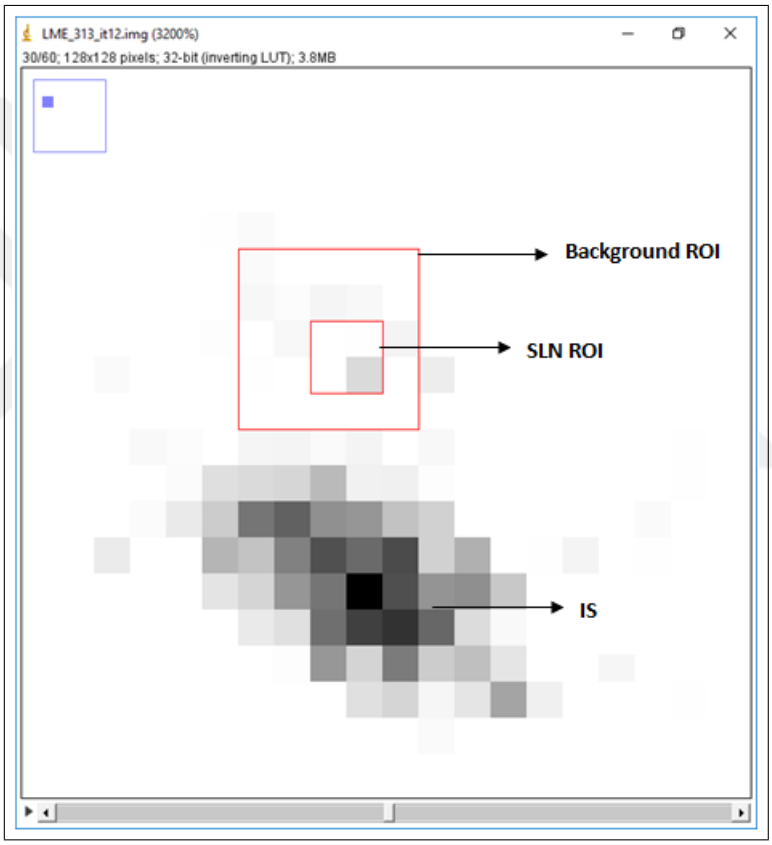

Figure 2.15 Illustration of SLN ROI, Background ROI, and IS.

3. RESULTS

The two samples (simind185, simind197) of **SIMIND** SPECT simulations for each collimator **(LEHR, LMEGP)** with poisson noise are depicted in Figure 3.1-Figure 3.10.

Figure 3.1 Simulation #: simind185, Collimator: LMEGP, Poisson noise added, Slice: 1/60.

The average **SLN** contrast values ($Mean \pm SD$) of a total number of 80 reconstructed images are given in Table 3.2 and illustrated in Figure 3.11, Figure 3.12 in terms of collimator type and correction method.

According to Table 3.1 the images projected by **LMEGP** collimator provided that the **SLN** contrast ($Mean \pm SD$) by attenuation correction resulted in the best

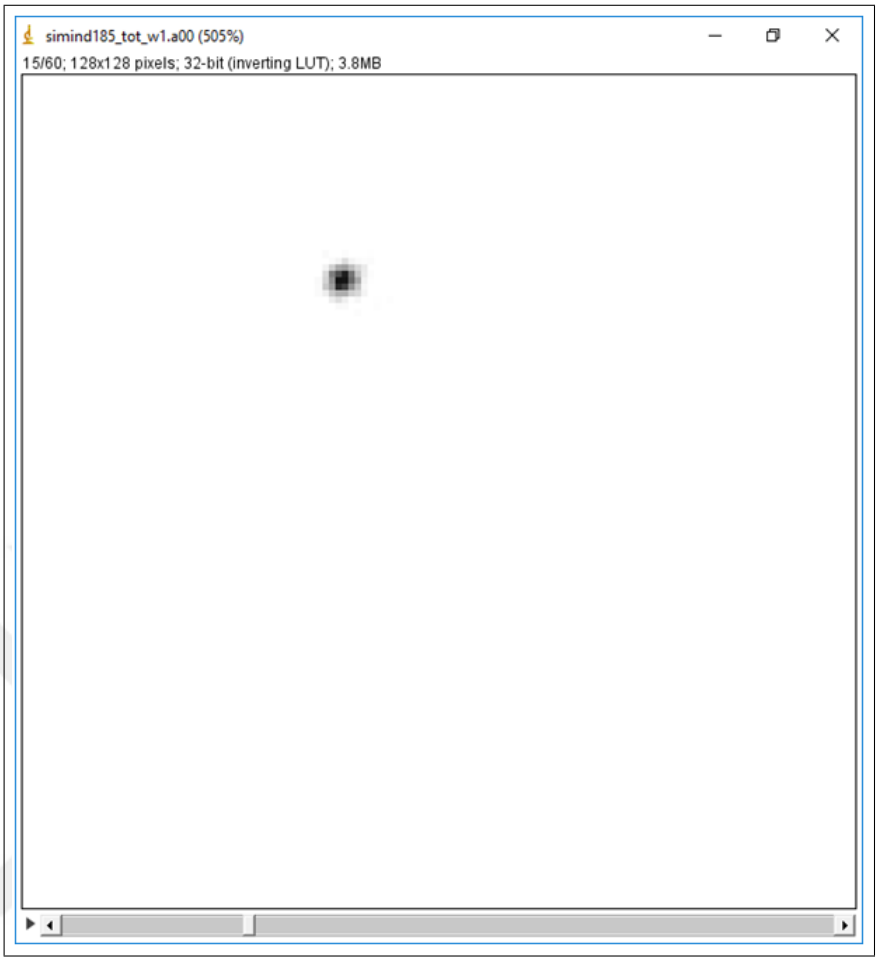

Figure 3.2 Simulation #: simind185, Collimator: LMEGP, Poisson noise added, Slice: 15/60.

contrast (0.4 ± 0.1), followed by the no correction (none) (0.3 ± 0.1), and the attenuation+scatter correction (0.3 ± 0.2). The contrast for the scatter correction was the lowest (0.1 ± 0.3). Significant ($p < 0.01$) average **SLN** contrast ratio [4 : 1] was obtained between attenuation and scatter correction methods for **LMEGP**. In addition significant differences were observed for **LMEGP** collimator between attenuation-none ($p \pm 0.01$) and none-scatter ($p = 0.01$) correction methods (Table 3.2).

SLN contrast results summarized in Table 3.1 for simulations using the **LEHR** collimator presented that with the best value of 0.4 ± 0.1 the attenuation correction method was in the first place, no correction (none) method was the second (0.3 ± 0.1) and attenuation+scatter correction (0.2 ± 0.1) was the third in terms of **SLN** detectability. Scatter correction method with an **SLN** contrast as 0.2 ± 0.3 was the

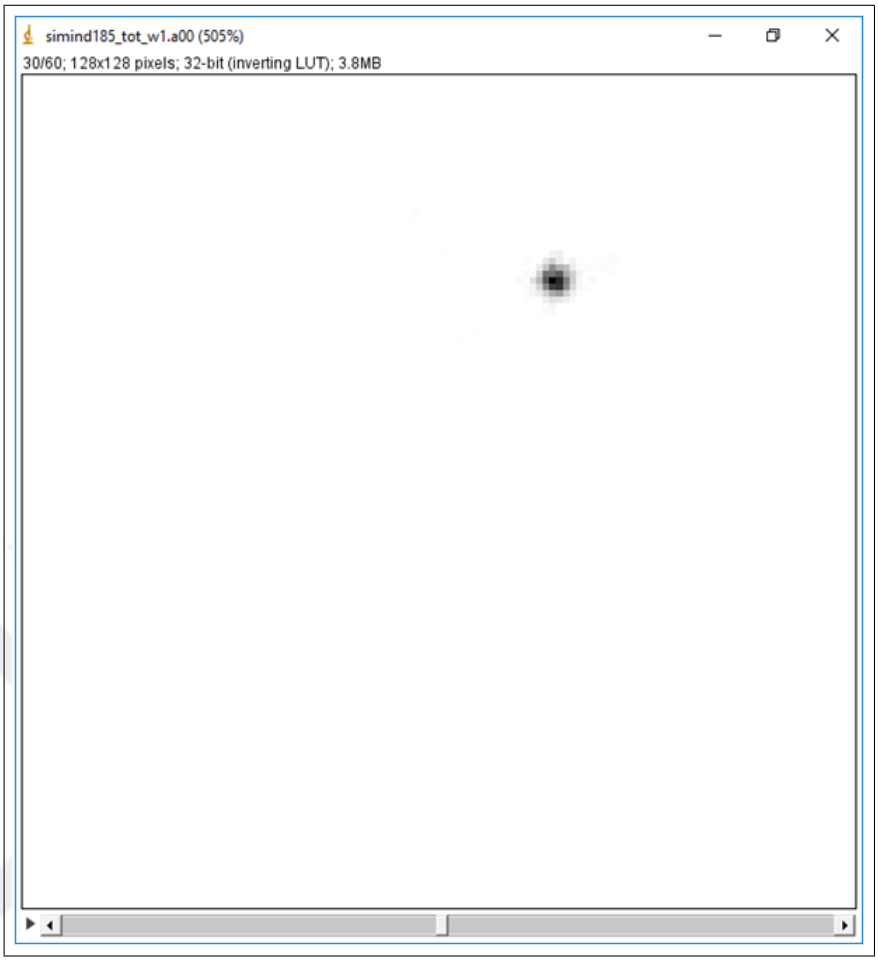

Figure 3.3 Simulation #: simind185, Collimator: LMEGP, Poisson noise added, Slice: 30/60.

worst among the four image correction methods. An important average **SLN** contrast difference was observed between attenuation and scatter correction methods with a ratio of [2 : 1] for **LEHR** collimator. Statistical significance among attenuation-none, attenuation-scatter, none-scatter reconstruction methods of **LEHR** collimator were observed as $p < 0.01$ (Table 3.3).

SLN average contrasts for attenuation and no correction (none) corrections methods were observed the same for both **LMEGP** and **LEHR** collimators. No significant statistical difference ($p > 0.1$) was observed between the two collimators incase of attenuation correction method was performed. **SLN** average contrast ($Mean \pm SD$) and significance values are depicted for **LMEGP** and **LEHR** collimators in Figure 3.11-Figure 3.12:

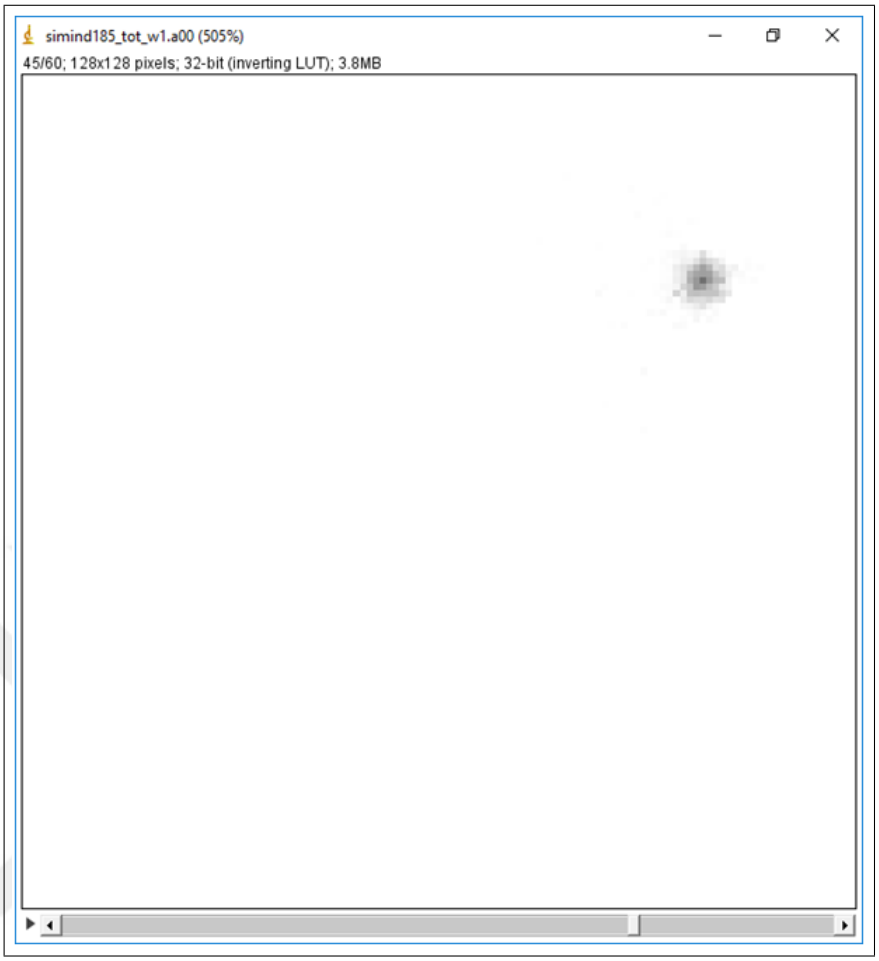

Figure 3.4 Simulation #: simind185, Collimator: LMEGP, Poisson noise added, Slice: 45/60.

Average counts ($Mean \pm SD$) of **SLNs** in **LEHR** and **LMEGP** SPECT images according to the reconstruction correction methods are summarized in Table 3.4.

The average **SLN** counts provided by the attenuation correction method was the highest (8749 ± 1347) for simulations using the **LMEGP** collimator, followed by the counts of the attenuation scatter (5374 ± 1610), and the no correction (none) (4981 ± 198) methods. The scatter correction **SLN** counts were the lowest (2349 ± 1270) (3.4). The simulations using the **LEHR** collimator resulted in the average counts **SLN** given in Table 3.4 regarding the correction method implemented from highest to lowest were attenuation correction (13456 ± 10753), attenuation+scatter correction (9411 ± 7816), no correction (none) (7854 ± 6472), and lastly scatter correction (4750 ± 3927). The standard deviations of the **SLN** counts in the images projected with **LEHR**

Figure 3.5 Simulation #: simind185, Collimator: LMEGP, Poisson noise added, Slice: 60/60.

collimator are observed considerably higher than their corresponding mean values and the standard deviations with the **LMEGP** collimator.

The effectiveness of both scatter and attenuation correction is summarized in Table 3.5:

According to the data presented in Table 3.5, the scatter correction effectiveness was calculated as 39% when attenuation + scatter correction method was compared with attenuation correction method and as 53% when scatter correction and no correction (none) correction methods were compared. The scatter correction effectiveness average was 46% for **LMEGP** collimator. For **LEHR** collimator these results were 30% and 40% respectively with an average of 35%. Attenuation correction effectiveness

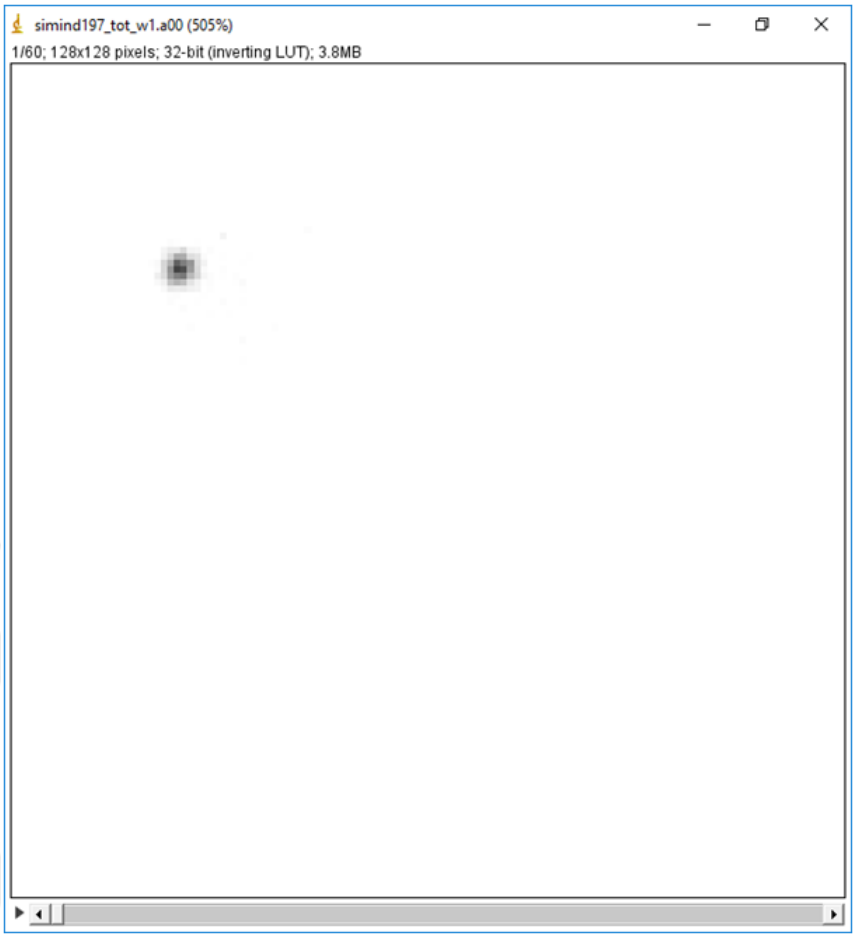

Figure 3.6 Simulation #: simind197, Collimator: LEHR, Poisson noise added, Slice: 1/60.

was calculated comparing the attenuation+scatter with scatter correction methods and attenuation with "none" correction methods. While the corresponding attenuation correction effectiveness were found as 129% and 76% accordingly with an average value as 103% for **LMEGP** collimator, for **LEHR** collimator 98%, and 71% results yielded an average of 85%. It is observed from the effectiveness data presented in Table 3.5 that attenuation correction had higher effect on **SLN** counts than scatter correction. According to the data in Table A.5 average sensitivity and penetration results of the **SIMIND** simulations using the **LMEGP** and **LEHR** collimators are summarized in Table 3.6.

According to Table 3.6 simulations using the **LEHR** collimator resulted in a higher average penetration rate (3.8%) than **LMEGP** collimator (2.5%). On the other

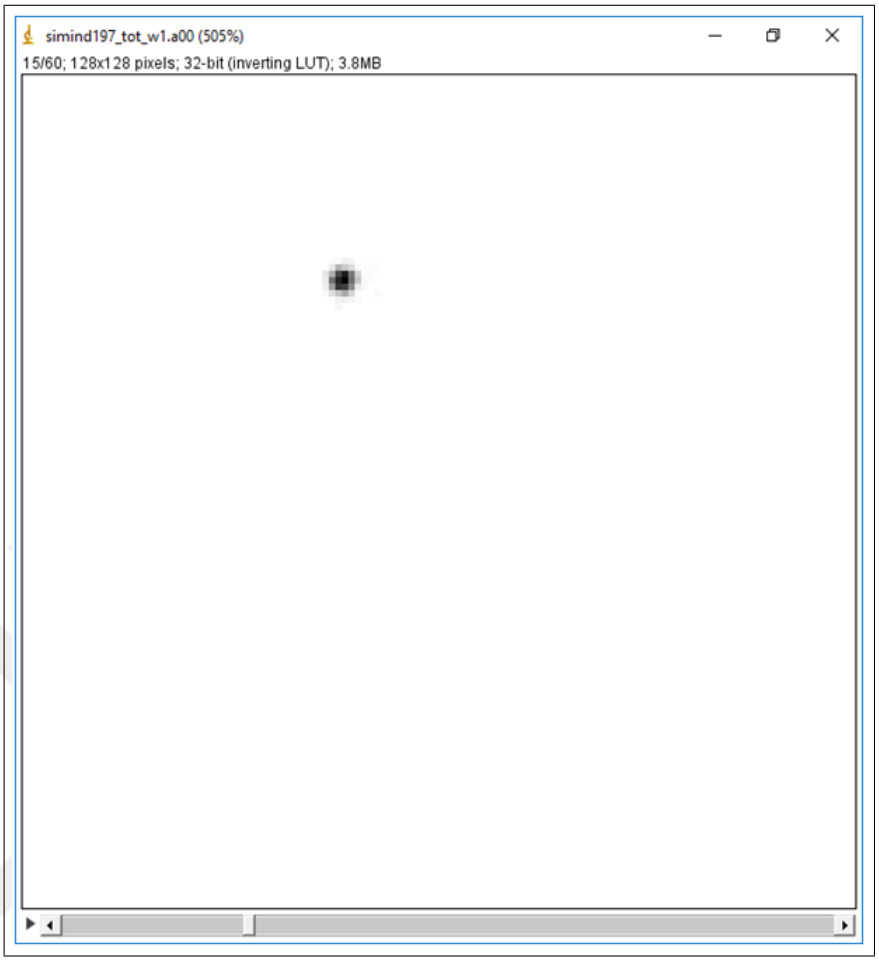

Figure 3.7 Simulation #: simind197, Collimator: LEHR, Poisson noise added, Slice: 15/60.

hand the **SIMIND** simulations reported a higher sensitivity for **LMEGP** collimator ($5.5 cpm/kBq$) than **LEHR** collimator ($3.1 cpm/kBq$) **(MIP)** of reconstructed images samples obtained by **LMEGP** collimator are illustrated in Figure 3.13-Figure 3.16.

(MIP) of reconstructed images samples obtained by **LEHR** collimator are illustrated in Figure 3.17-Figure 3.20.

(MIP) of reconstructed images with the highest contrasts performed using attenuation correction method for **LMEGP** and **LEHR** collimators are illustrated in Figure 3.21 and Figure 3.22.

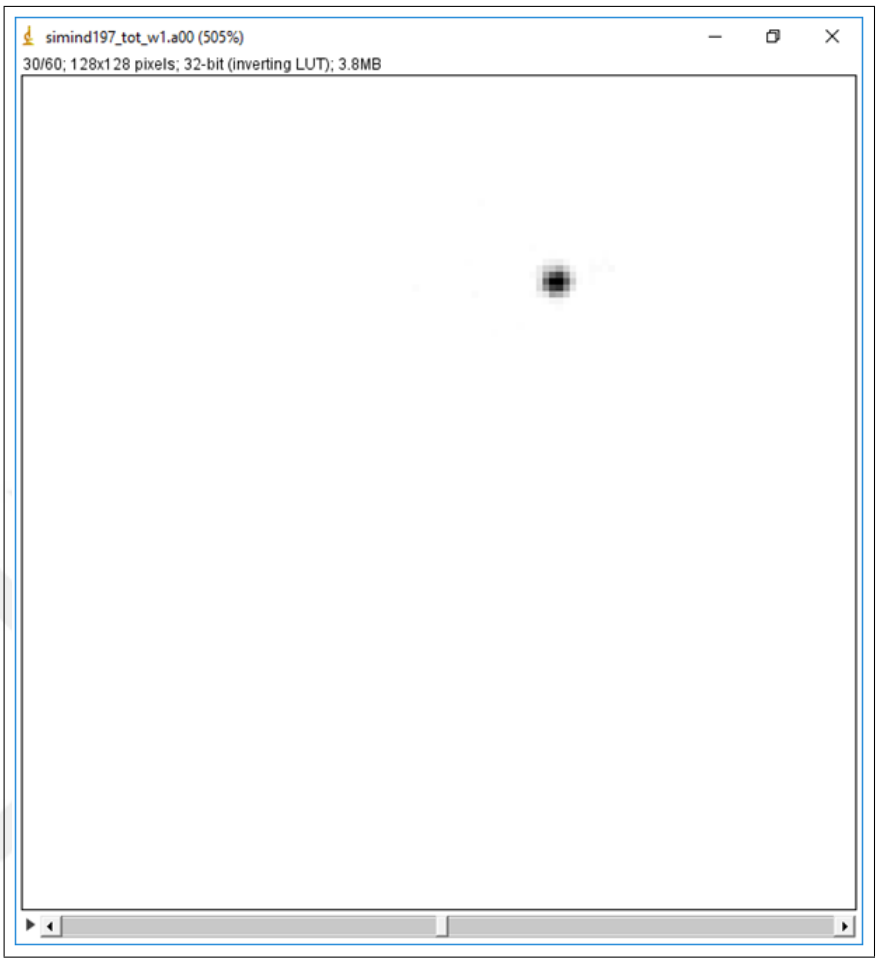

Figure 3.8 Simulation #: simind197, Collimator: LEHR, Poisson noise added, Slice: 30/60.

Table 3.1
Average SLN Contrasts of Correction Methods applied in SPECT Simulations using the LMEGP and LEHR Collimators.

Correction Method	**SLN Contrast** (LMEGP)	**SLN Contrast** (LEHR)
Attenuation	0.4 ±0.1	0.4 ±0.1
None	0.3 ±0.1	0.3 ±0.1
Scatter	0.1 ±0.3	0.2 ±0.3
Attenuation+Scatter	0.3 ±0.2	0.3 ±0.3

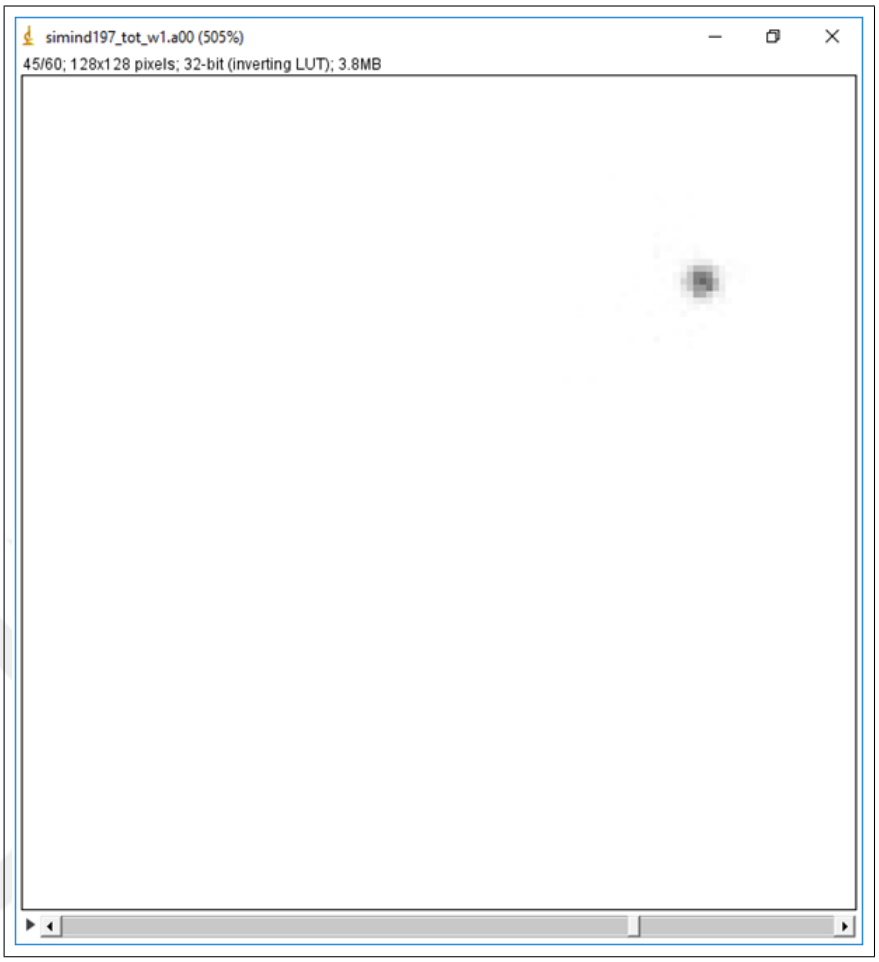

Figure 3.9 Simulation #: simind197, Collimator: LEHR, Poisson noise added, Slice: 45/60.

Table 3.2
p values for LMEGP Collimator.

Correction Method	**None**	**Scatter**
Attenuation	0.01	< 0.01
None	$--$	0.01

Table 3.3
p values for LEHR Collimator.

Correction Method	**None**	**Scatter**
Attenuation	< 0.01	< 0.01
None	$--$	< 0.01

Figure 3.10 Simulation #: simind197, Collimator: LEHR, Poisson noise added, Slice: 60/60.

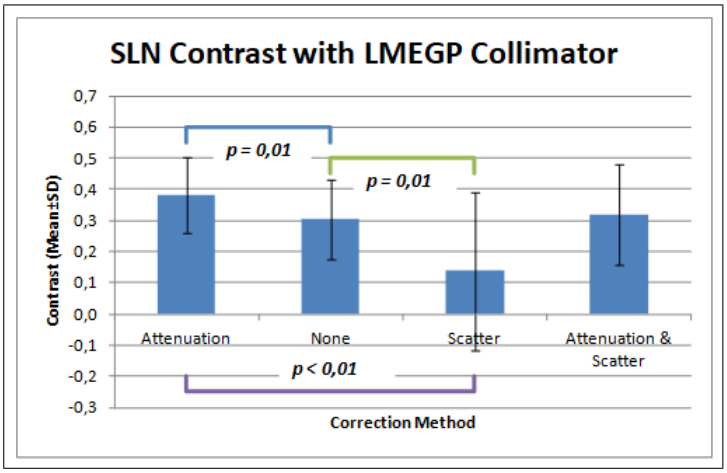

Figure 3.11 Average SLN Contrasts of Correction Methods applied in SPECT Simulations using the LMEGP Collimator.

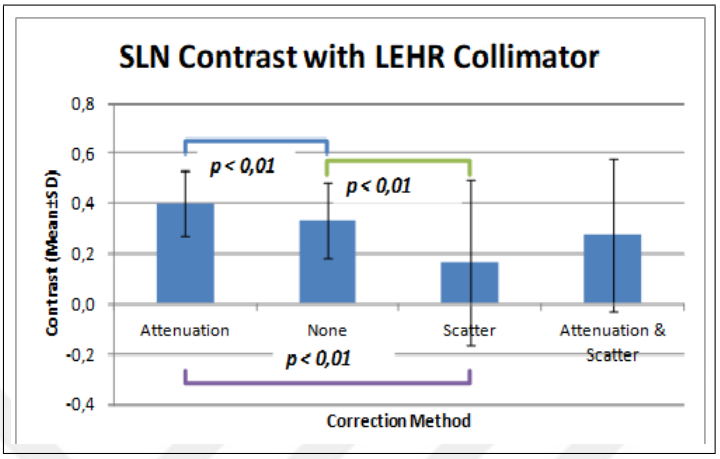

Figure 3.12 Average SLN Contrasts of Correction Methods applied in SPECT Simulations using the LEHR Collimator.

Table 3.4
Average SLN Counts of Correction Methods applied in SPECT Simulations using the LMEGP and LEHR Collimators.

Correction Method	**SLN Count (LMEGP)**	**SLN Count (LEHR)**
Attenuation	8749 ±1347	13456 ±10753
None	4981 ±198	7854 ±6472
Scatter	2349 ±1270	4750 ±3927
Attenuation+Scatter	5374 ±1610	9411 ±7816

Table 3.5
Scatter and Attenuation Correction Effectiveness.

Comparison of Correction Methods	**Scatter Correction Effectiveness**		**Attenuation Correction Effectiveness**	
	LMEGP	**LEHR**	**LMEGP**	**LEHR**
Attenuation vs Attenuation+Scatter	39%	30%	−−	−−
None vs Scatter	53%	40%	−−	−−
Scatter vs Attenuation+Scatter	−−	−−	129%	98%
None vs Attenuation	−−	−−	76%	71%

Table 3.6
Sensitivity and Penetration Results of the Simulations.

Collimator Type	**Sensitivity** (cpm/kBq)	**Penetration (%) After Collimator**
LMEGP	5.5	2.5
LEHR	3.1	3.8

Figure 3.13 Reconstruction #: LMEGP_302, Correction Method: None, MIP image, Contrast: 0.33.

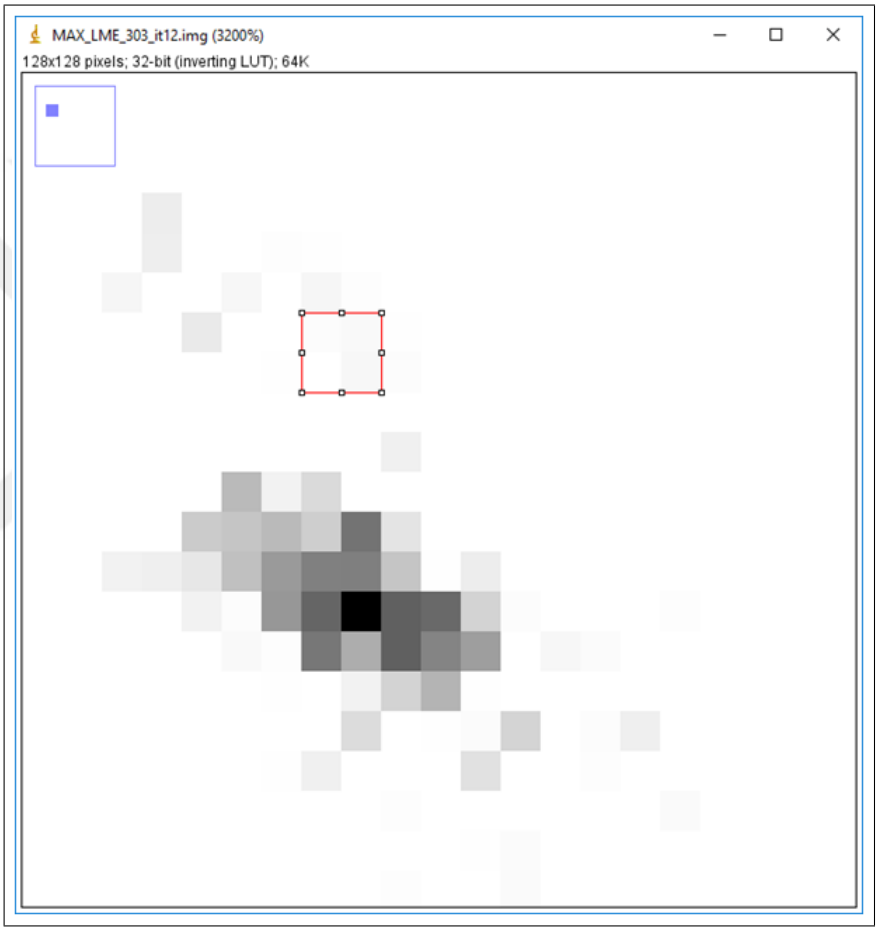

Figure 3.14 Reconstruction #: LMEGP_303, Correction Method: Attenuation, MIP image, SLN Contrast: 0.43.

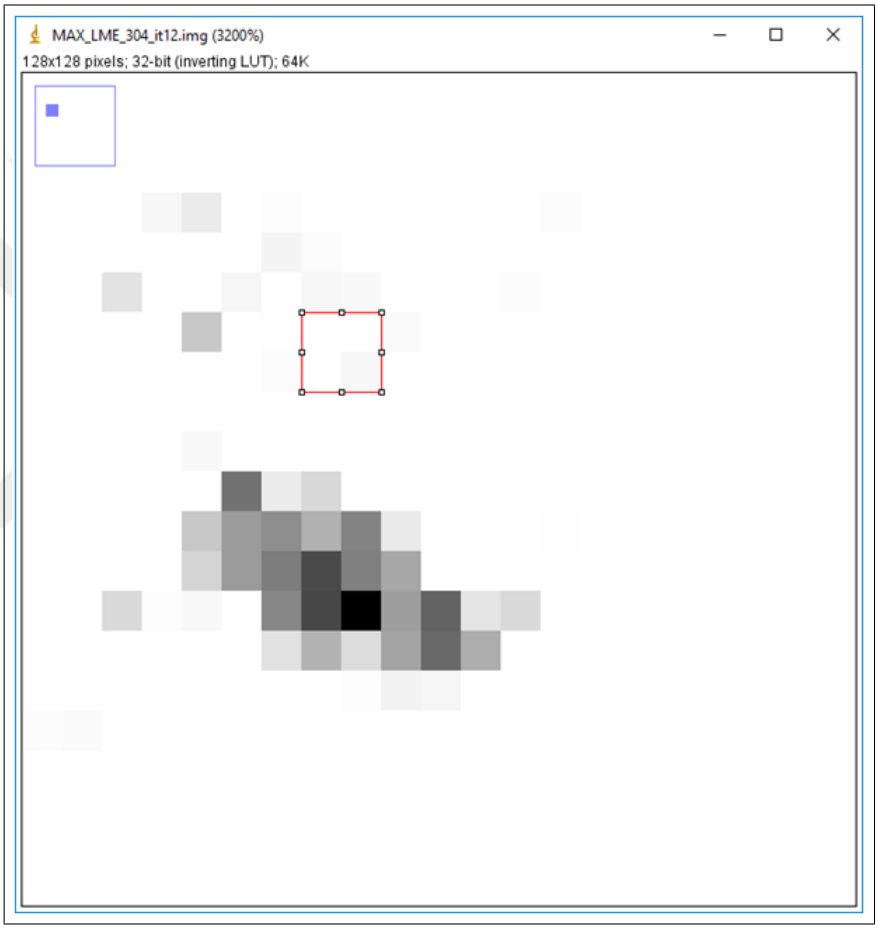

Figure 3.15 Reconstruction #: LMEGP_304, Correction Method: Scatter, MIP image, Contrast: 0.03.

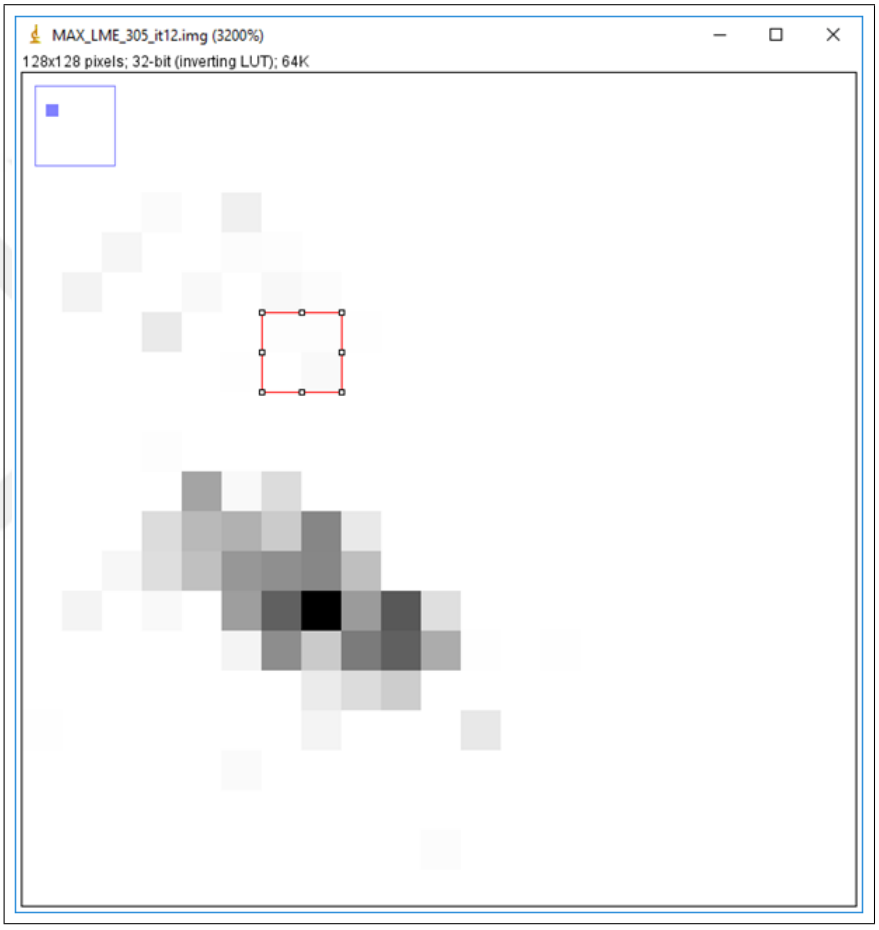

Figure 3.16 Reconstruction #: LMEGP_305, Correction Method: Attenuation+Scatter, MIP image, Contrast: 0.29.

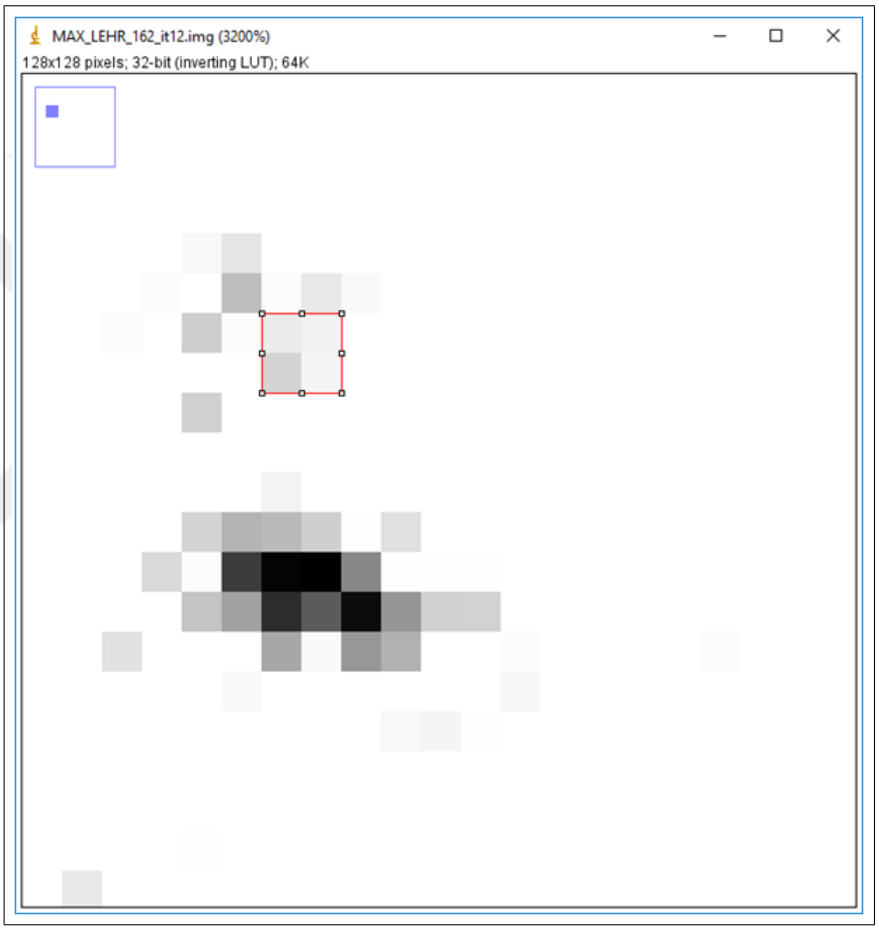

Figure 3.17 Reconstruction #: LEHR_162, Correction Method: None, MIP image, Contrast: 0.26.

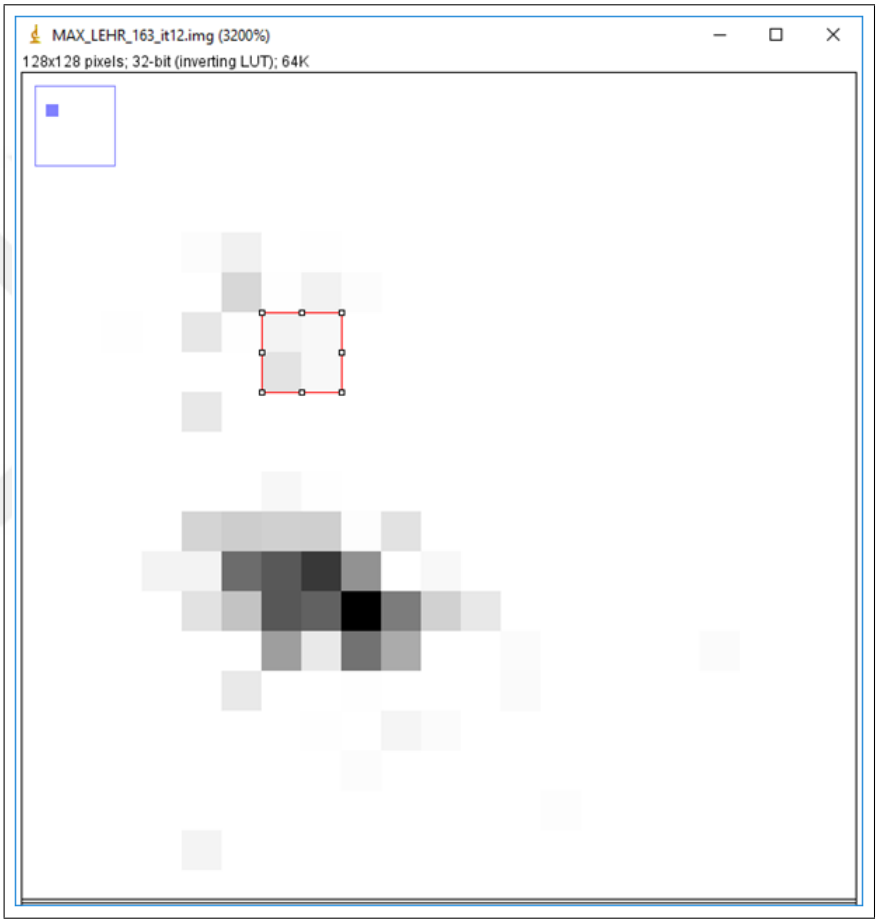

Figure 3.18 Reconstruction #: LEHR_163, Correction Method: Attenuation, MIP image, Contrast: 0.31.

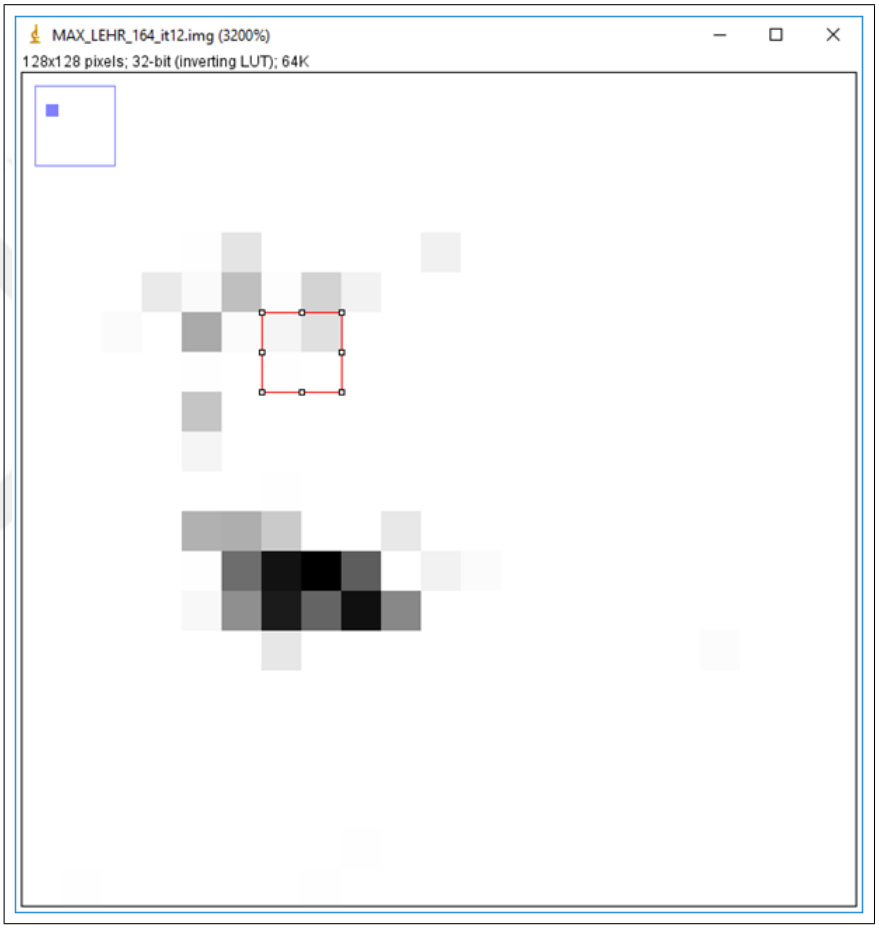

Figure 3.19 Reconstruction #: LEHR_164, Correction Method: Scatter, MIP image, Contrast: -0,12.

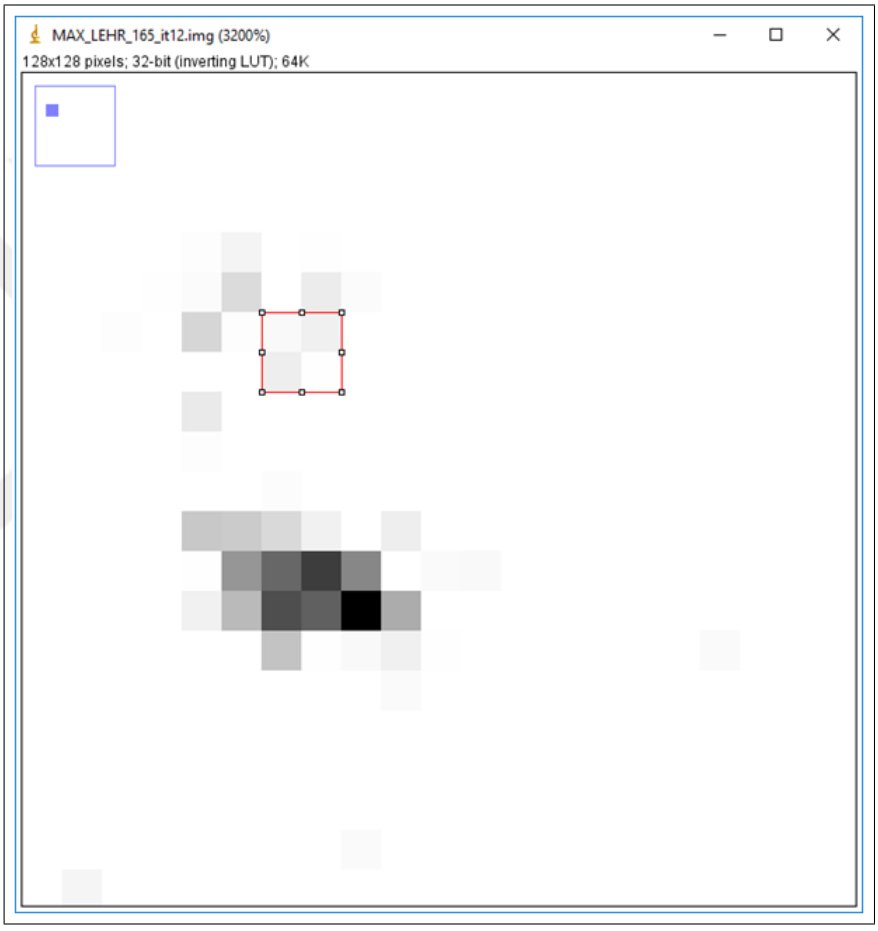

Figure 3.20 Reconstruction #: LEHR_165, Correction Method: Attenuation+Scatter, MIP image, Contrast: 0.16.

Figure 3.21 Reconstruction #: LMEGP_298, Correction Method: Attenuation, MIP image, and Contrast: 0.54.

Figure 3.22 Reconstruction #: LEHR_171, Correction Method: Attenuation, MIP image, Contrast: 0.58.

4. DISCUSSION

It is observed from Table 3.1, Figure 3.11, and Figure 3.12 that attenuation correction resulted in the highest contrast (0.4 ± 0.1) with a significance $p \leq 0.01$ for both collimators **(LMEGP, LEHR)** when compared with no correction (none) and scatter reconstruction methods. Therefore, attenuation correction can be defined as the optimum reconstruction method for **LMEGP** and **LEHR** collimators. Considering the contrast standard deviation (SD) together with the averages, performing no correction is in the second place with a contrast of 0.3 ± 0.1. There was significant difference between the "none" and scatter correction method ($p \leq 0.01$). Because of the higher SD, attenuation+scatter correction method is in the third place with a contrast value as 0.3 ± 0.2 for **LMEGP** collimator and 0.3 ± 0.3 for **LEHR** collimator. There was no statistically significant difference (p>0,01) observed between attenuation+scatter and other correction methods. Scatter correction yielded significantly ($p \leq 0.01$) the worst **SLN** contrasts (0.1 ± 0.3) for **LMEGP** collimator and 0.2 ± 0.3 for **LEHR** collimator when compared with other correction methods. These results might mean that attenuation correction is the optimum reconstruction correction method for the SPECT images projected by both **LEHR** and **LMEGP** collimators. It can be further concluded from the study results that without an attenuation correction no significant benefit on **SLN** visualization could be expected from scatter correction alone.

In the comparison of the **SLN** contrasts of **LMEGP** and **LEHR** collimators when the suggested optimum correction method (attenuation correction) is implemented to SPECT images, contrasts were calculated as the same (0.4 ± 0.1) for both collimators after the 10^{th} simulation trial for each collimator. The contrast results of **LMEGP** and **LEHR** collimators have no statistically significant difference ($p > 0.1$) in case of attenuation correction.

Even if the input parameters are the same for the **SIMIND** simulations performed using these two **LMEGP**, LEHR collimators as a result of the randomness

base of the Monte Carlo simulations by each **SIMIND** simulation varying contrast results were obtained. This situation leaded the study to decide the sample size for the simulations (which was decided as 10 simulations per each collimator) and to take the cumulative averages of the **SLN ROI** counts, **SLN Background ROI** counts and contrasts for the total 10 simulations.

The average **SLN** counts regarding **LMEGP** and **LEHR** simulations presented in Table 3.4 are maximum with attenuation correction followed by attenuation+ scatter correction and without any correction method. Scatter correction alone resulted in the least **SLN** counts for both collimators. The decrease in **SLN** counts with scatter correction and increase in **SLN** counts with attenuation correction can be called as expected. The **SLN** counts in images projected by **LEHR** collimator are higher than the **SLN** counts with **LMEGP** collimator. On the other hand it is also observed from the Table 3.4 that standard deviations of the **SLN** counts in images with **LEHR** collimator are also considerably higher when compared with the standard deviations of the **SLN** counts with **LMEGP** collimator. The sequence of average **SLN** counts of both **LMEGP** and **LEHR** collimators from highest to lowest as attenuation correction, attenuation+scatter correction, no correction (none), and scatter correction respectively is in line with the study of Yoneyama at al [4].The magnitude of the **SLN** average counts are correlated between the two studies. This is due to the activity normalization applied during reconstruction aiming to have comparable **SLN** counts and **SLN** contrasts with the study of Yoneyama at al [4].

Lower and negative contrasts are caused by the higher mean value of **Background ROI** than **SLN ROI**. Even though it is reported that **SLN to background ratio** is at least 10 : 1, being very closed to an **IS** with most of the injected activity might be the reason for these results.

Comparing the contrast results of the attenuation corrected images with attenuation+scatter corrected images for both **LMEGP** and **LEHR** collimators it can be concluded that if attenuation correction is implemented the additional scatter correction implementation might decrease the **SLN** detectability in terms of contrast.

In addition higher standard deviation of the contrast values for attenuation+scatter corrected images projected by **LMEGP** and **LEHR** collimators could name attenuation+scatter method less dependable against the choice of no correction (none) method.

It is significant in Table 3.1 that the scatter correction alone has the lowest contrast average and the highest standard deviation for both **LMEGP** and **LEHR** collimators 0.1 ± 0.3 and 0.2 ± 0.3 respectively among the total methods (attenuation, none, scatter, and attenuation+scatter). These results suggest that scatter correction alone should not be performed for **SLN SPECT** imaging when **SLNs** are located closed to the **ISs**.

Reconstruction with attenuation correction resulted in the highest contrast values therefore, this method was found to be the optimum reconstruction method for both **LMEGP** and **LEHR** collimators during **SLN** mapping with SPECT/CT.

It can be concluded that the visual interpretation of **MIP** images might not yield confident results. Because even in the attenuation corrected **LMEGP** and **LEHR** images (Figure 3.21, Figure 3.22) with the highest contrasts measured in the study (0.54, 0.58 respectively) the **SLNs** cannot be visually detected precisely in the images. Tsushima, Hiroyuki, et al. [26] reported in their study that image contrast of 0.5 which corresponds to a $3:1$ **SLN to background ratio** was a suitable threshold level for hot **SLN** detection. The maximum contrast of this study is (0.58) not so higher than the 0.5 threshold therefore the unprecise detection of **SLN** in the study might be regarded as an expected result.

SPECT systems are regarded as photon poor systems [36] as more than 99% of all the photons emitted by an injected radiopharmaceutical are not recorded by the gamma camera and "wasted"; only less than 1% are used for generating the desired image [37]. Therefore increasing collimator sensitivity is a crucial consideration for SPECT imaging. Sensitivity improvement (increased counts) of a collimator is dependent on the larger hole diameter and the smaller septa/hole length. According to the Table 2.5 the hole diameter of the **LMEGP** collimator ($2.70mm$) is nearly

2.4 folds of **LEHR** collimator ($1.11mm$) on the other hand the septa/hole length of the **LMEGP** ($37mm$) collimator is nearly 1.5 times greater that **LEHR** collimator septa/hole length. The average sensitivity (cpm/kBq) calculated for **LMEGP** and **LEHR** collimators are 5.5 and 3.1 respectively which means the sensitivity ratio between **LMEGP** and **LEHR** collimators (5.5 : 3.1) is approximately 1.8 (Table 3.6). In Table 2.5 where vendor collimator specifications are given sensitivity (cpm/kBq) of **LMEGP** collimator (9.2) is 1.7 folds of **LEHR** collimator (5.5). Sensitivity ratio of the collimators are nearly the same both vendor supplied data and the results of the study. It can be inferred from the septa/hole length, hole diameter input parameters, and the sensitivity results of the collimators that larger hole diameter advantage of **LMEGP** collimator compensated its longer septa/hole length disadvantage and yielded a better sensitivity value than **LEHR** collimator.

The higher average **SLN** counts of the images projected with **LEHR** collimator compared to those with **LMEGP** collimator presented in Table 3.4 can be seen as controversial with the collimator sensitivity results presented in Table 3.6. The explanation of this issue is collimator sensitivity results are based on the simulations and the **SLN** counts are based on the reconstructed images. Because Yoneyama et al. [4] presented average counts ($Mean \pm SD$) of **SLNs** in SPECT/CT images projected by **LMEGP** collimator but did not report SLN counts for **LEHR** collimator in their previous study [16]. In this study the **SLN** counts of the reconstructed images projected with **LMEGP** collimator were normalized to mentioned count data in the study of Yoneyama et al. [4]. This normalization was performed with the activity adjustment index **(MB)** of the **smc2castor program**. The same **LMEGP** collimator specific **(MB)** switch was used for the reconstruction of the corresponding **LEHR** collimator projected images. For instance during the reconstructions of the first **LMEGP** and **LEHR** simulations the same **(MB)** switch specific to the first **LMEGP** simulation was used. As **MB** switch has a linear effect on the **SLN** count outcomes of the reconstructions and contrast value (the focus of our study) is independent of related counts, having a lower sensitivity in Table 3.6 but having higher **SLN** counts in Table 3.4 should not be seen controversial phenomena for **LEHR** collimator and for the study.

Septal penetration ratio of collimators while increasing the background counts also reduces the contrast. Septal penetration depends on the septal thickness of the collimators and the energy of the emitted photons. As study of interest radionuclide is the same (Tc^{99m}) for both **LMEGP** and **LEHR** collimators the septal thickness parameter takes precedence in septal penetration ratio assuming that total number of collimator holes is the same for each collimator. Thicker septal thickness results in reduced septal penetration ratio. According to the collimator specifications data in Table 2.5 the septal thickness of **LMEGP** collimator ($0.6mm$) is 3.8 times greater than the septal thickness of **LEHR** collimator (0.16). According to Table 3.6 calculated penetration ratio of **LEHR** collimator (3.8%) is 1.5 times greater than the **LMEGP** collimator (2.5%). In Table 2.5 where vendor collimator specifications are given penetration ratio of **LEHR** collimator (1%) is more than 10 times greater than the **LMEGP** collimator (0.1%. Although Tc^{99m} is classified as low energy photon and might not be expected to be affected by the septal thickness change because of its low energy it can be concluded from this study that larger septal thickness characteristics leading to lower septal penetration of **LMEGP** collimator might be the reason for improved and competitive **SLN** contrast results against **LEHR** collimator with higher septal penetration ratio caused by smaller septal thickness.

Resolution and sensitivity performance of a collimator is inversely proportional. In this study **LMEGP** collimator could compensate their lower resolution characteristics with lower septal penetration and with higher sensitivity and could present competitive **SLN** contrast levels as compared with **LEHR** collimator. The findings concerning collimator sensitivity and penetration are in line with the data presented in Table 2.5.

In this study according the physical phantom study of Yoneyama et al. [16] $1.6cm$ ($4pixels$) in diameter and $0.8cm$ ($2pixels$) thick cylindrical **IS**; and a $0.8cm$ ($2pixels$) in diameter and $0.8cm$ ($2pixels$) thick cylindrical **SLN** were modeled. According to the histological data of Farshid, Gelareh, et al. [38] an **SLN** width ranges between $0.5mm$ and $15mm$ with a mean of $5.14mm$, and an **SLN** length ranges between $0.5mm$ and $27mm$ with a mean of $8.47mm$. It can be concluded that the **IS** and

SLN dimensions in this study are also in line with the report of Farshid, Gelareh, et al. [38].

The **IS:SLN** activity ratio in this study was selected as 250 : 10 among the **IS:SLN** ratios applied in the study of Yoneyama et al. [16]. 250 : 10 **IS:SLN** ratio complies with the investigation findings of Alqahtani, M. S., et al. [39] declaring that in the majority of the studies 1 : 20, 1 : 50, and 1 : 100 **SLN:IS** activity uptake ratios are used.

Yoneyama et al. [4] reported that the average distance between the **SLN** and body surface was $2.6 \pm 1.3cm$ ($median 2.2cm$) in their study. Therefore 1.5 cm **SLN-body** distance in this study can be regarded as a reasonable distance when compared with their findings. In the same study [4] they measured the average distance of **SLN** to the **IS** in their clinical study cohort as $7.6 \pm 2.6cm$ ($median 7.3cm$). In their previous physical phantom study Yoneyama et al. [16] compared the **SLN** contrast values of different collimators **(LMEGP, LEHR, and ME)** for both $3cm$ and $6cm$ **IS-SLN** distances. With the $3cm$ **IS-SLN** distance they simulated the effect on contrast for an **SLN** being closed to and **ISs**. As non visualization of **SLNs** concerning their being in close proximity to injection sites is one of the reasons of supplementary SPECT/CT imaging to lymphoscintigraphy is chosen in this study **SLN** was located close to injection site ($3cm$). The **IS-SLN** distance of $3cm$ also made the results of the study comparable with the results of Yoneyama et al. [16].

Yoneyama et al. [4] correlated the effect of scatter correction in relation with the distance between **SLNs** and **IS** and the effect of attenuation correction regarding the distance between the **SLNs** and the body surface in their clinical study over 55 female patients. From the related graphics in their report [4] it can be deduced that for a $1.5cm$ distance between **SLN** and body surface the attenuation effect was interpreted as approximately 85% and for a $7cm$ **SLN-IS** distance the effect of scatter correction was predicted as approximately 40% for **LMEGP** collimator. It can be concluded that both attenuation and scatter correction effectiveness estimated in this study are in close proximity with the study of Yoneyama et al. [4].

According to their physical phantom study Yoneyama et al. [16] suggested that in case of attenuation correction was selected as the image reconstruction correction method, **LMEGP** collimator might result in higher contrast and improve the **SLN** detectability than **LEHR** collimator. In this study with a sample size of 10 **SIMIND** simulations for each collimator **(LMEGP, LEHR)** the cumulative average **SLN** contrast ($Mean \pm SD$) was calculated the same (0.4 ± 0.1) for both collimators. As according to the guideline for lymphoscintigraphy and sentinel node localization in breast cancer [12] **LEHR** and **LEUHR** collimators are the only recommended collimators for both lymphoscintigraphy and SPECT/CT imaging because of their high resolution characteristics and suitability for radionuclides with low energy such as Tc^{99m}. This study presented that **LMEGP** collimator could compensate its lower resolution characteristics with its lower septal penetration advantage and could be competitive in terms of **SLN** detectability against **LEHR** collimator. Yoneyama et al. [4] performed resolution correction in their study with **LMEGP** collimator.

In our study as there was no resolution correction capability of the reconstruction program **(CASToR)**, resolution correction could not be performed. In order to have comparable contrast results with the study of Yoneyama et al. [4] that implemented resolution correction the number of projections were increased [12] to 120 projections instead of the 60 projections implemented in their study.

It can be inferred that it might be probable to have a higher **SLN** contrast with **LMEGP** collimator than **LEHR** collimator if resolution correction could be performed in addition to attenuation correction. It can be summarized that the results of this study are in agreement with the studies performed by Yoneyama et al. [4, 16].

In the literature [6, 12, 40, 41, 42] **SLN** radioactivity uptake quantification is regarded as clinically not required or useful because of naming a lymph node as an **SLN** is not correlated with the amount of the radioactivity uptake in it. Therefore anatomical localization of the radionuclide uptake is more favored than its quantification. However in this study the **SLN** counts of the reconstructed images regarding varying correction methods to be in line with the counts reported in reference study [4]

was the primary aim in order to offer comparable results with those in the literature.

In this study an extreme case in which an **SLN** with small activity is located closely to **IS** with high radioactivity (**IS:SLN** activity ratio as 250/10). Because of the scattering of the photons originating from **IS** to the **SLN** in closed proximity average **SLN** contrasts were expected as low. According to the Table 3.1 the average **SLN** contrasts ($Mean \pm SD$) of correction methods applied in SPECT simulations using the **LMEGP** and **LEHR** collimators are in the range of 0.1 ± 0.3 - 0.4 ± 0.1. **SLN-to-background** radioactivity ratios in vivo are typically on the order of 3 : 1, 10 : 1, 15 : 1, or even 20 : 1 in the literature [40, 43, 39, 44]. According to the contrast formula (Eq. 2.1) **SLN-to-background** ratios correspond to a contrast value in a range of $0.5 - 0.9$. As an extreme case of **SLN** being closed to **IS** was modeled in the study and this case might cause a decrease in the contrast values it can be concluded that the **SLN** contrast results of this study in Table 3.1 might be considered as compatible with the general in vivo **SLN-to-background** ratio in the literature.

Because there is only one **SLN** modeled near an **IS**, a star shaped artifact originating from the scattering of the **IS** similar to the physical phantom study of Yoneyama et al. [16] could not be observed in the study.

High-resolution collimators are recommended for improving lymphoscintigraphy images [40].

There were a number constraints in the study which can be grouped as availability of relevant clinical or phantom study data, the capability of Monte Carlo SPECT simulation **(SIMIND)** and reconstruction **(CASToR)** program, and simulation sample size.

In order to have realistic results from simulation studies adequate, complete, and accurate data representing the real world is a prerequisite. The potential data sources are especially the clinical and phantom studies. In the field of this study (SPECT imaging of axillary **SLNs** in breast cancer) the investigations were limited

[4, 16] so the input parameters of SPECT simulations were dependent on these few data in the literature. For example although a dual energy window for scatter correction was referred in their second study [16] the energy windows and the scatter constant ($kfactor$) were not explained. Therefore the range of the scatter windows and the scatter constant were defined in the study by tailoring general literature concerning the dual energy window. Nevertheless as these two studies [4, 16] are complementary with each other the input, method and results presented in their reports affected the outcomes of this study in a positive way. It was observed that the **LMEGP** collimator is not a common collimator in nuclear imaging and the studies are limited including the investigations of Yoneyama et al. [4, 16]. The nonavailability of the collimator specifications data of **LMEGP** was overcome by using the low-medium-energy **(LME)** collimator data given in the study of Inoue, Yusuke, et al. [29] assuming that **(LME)** and **LMEGP** are most likely the same collimators but only their notations are different in the related studies [4, 16, 29]. In addition **SIMIND** program does not include the **LMEGP** collimator in its database. **LMEGP** collimator has been included to the CHANGE according to the **SIMIND** Manual [27]. Because of an inconvenience of **SIMIND** program to define the newly added collimator name in the CHANGE program simulation reports were released with a collimator name as **SY-ME**. As it can be observed in Figure 2.10 and Figure A.1 manual correction of the collimator name as **LMEGP** has been done in these figure and report.

The availability, functional capabilities, easiness, and reputation of simulation tools (programs, phantoms etc) determine how extent the study input data could be modeled and simulated in a sufficient manner. For instance Yoneyama et al. [4, 16] used a fixed attenuation coefficient ($\mu = 0.15cm^{-1}$) while in this study **SIMIND** used an aligned attenuation map created from a user-specified input file [27]during attenuation correction.

Yoneyama et al. [4] implemented resolution correction in order to have similar resolutions between the **LMEGP** and **LEHR** collimators as resolution of the **LMEGP** collimator is less than **LEHR** collimator. **CASToR** program had only attenuation and scatter correction capability therefore resolution correction could not be performed and

the effect of resolution correction on the **SLN** detectability could not be observed. Even it is a newly released tool and therefore might not be a reputable software at the time of study, using **CASToR** [23] as a reconstruction tool decision was based on the availability of **SIMIND** conversion program called **smc2castor** which facilitated to reconstruct **SIMIND** simulations [27].

In order to reduce the artifacts in images Yoneyama et al. [4, 16] implemented ordered subset expectation maximization **(OSEM)** iterative reconstruction algorithm with 12 iterations and 15 subsets. On the other hand in the study image reconstructions were performed by **CASToR** program using maximum likelihood expectation maximization **(MLEM)** reconstruction algorithm with 12 iterations and 15 subsets. **OSEM** algorithm is a block-iterative version of **MLEM** developed in order to improve the speed of **MLEM** algorithms which are computationally intensive. They are the most widely used technique on commercial nuclear medicine computer systems and have been in use for routine clinical practice [45, 46].

The most important limitations of this study were about the phantom used. **SIMIND** Monte Carlo program [19] supports lots of phantom models and the **ZUBAL** [18] torso phantom with no arms and legs is one of the most widely used phantom in research. Although it is very easy to make realistic studies over this anthropomorphic phantom by **SIMIND** as this phantom was created from sets of segmented images of living human males it was very difficult to model a female patient with breast cancer and to locate the **SLN** and **IS** in the phantom because of lack of appropriate breast organ structure in the human male phantom compared to human females. Most of the clinical studies in the literature together with the ones [4, 16] which were the origin of this study are mostly focused on female breast cancer patients. The risk of using a male anthropomorphic phantom could be mitigated with the data reported in the literature [5] that between female and male breasts there was no significant difference.

The second important limiting factor for this study was that the activity uptake of soft tissues such as fat, muscle, skin which spread all over the body cannot be confined around the study of interest. Therefore in this study it was not able to define

and implement an **SLN** to background activity ratio for fat and muscle tissues around the axilla and the relative activities in the simind.zub file were zeroized. This the most important constraint of the study which caused to model only **SLN** and **IS** and ignore the activity effects of the surrounding tissue (background) of the **SLN**. Nevertheless because in this study one of the extreme cases (an **SLN** in closed proximity to **IS**) which necessitates additional SPECT/CT imaging to lymphoscintigraphy was modeled, the negative effect of this important constraint was mitigated. As **simind.zub** file is used for both activitiy and density maps, densities of the organs defined in **simind.zub** file enabled attenuation and scatter corrections even though the relative activities of the organs were ignored and zeroized.

Lastly, the simulation tools are black box solutions therefore even the simulation input can be changed there is no possibility to interfere with the underlying algorithm, physics of these tools and the study results are shaped according to the intrinsic structure of them. Therefore using well-known, reputable simulation tools is of essential importance.

The decision of sample size of a simulation study is influenced by the fluctuations or standard deviations of each simulation run and the time that can be devoted to the study. Because of the randomness nature of Monte Carlo simulations a varying output in spite of the same input is an expected thing. In order to decide on an effective simulation sample size in terms of output data dependability (quality of data) and the elapsed time, cumulative averages of the results were traced after each subsequent simulation and simulations were stopped when cumulative of the averages observed as stable. Even though the more sample means more reliable results considering the time limit 10 simulations for each collimator **(LMEGP and LEHR)** as a SPECT simulation sample was decided as adequate in this study.

Eliminating or mitigating the limitations experienced in this study might yield more realistic results for the next simulation studies in simulation and optimization of **SLN** mapping with **SPECT** imaging regarding breast cancer.

The method presented in this study will enable further Monte Carlo simulation studies with digital anthropomorphic phantoms concerning the optimization of multiple acquisition and processing parameters of **SLN SPECT** imaging such as different gamma camera(s), collimator settings, patient dimensions, and reconstruction correction methods (attenuation, scatter) in breast cancer examinations realistically, accurately and at a lower cost than physical phantom or clinical studies. The dependable results of these simulation studies will support and guide the subsequent patient and phantom studies and increase the effectiveness of their outcomes.

5. CONCLUSIONS

In order to improve the preoperative **SLN** mapping in breast cancer staging using SPECT/CT imaging, the aim of this study was to simulate and optimize **SLN** detectability optimization depending on various reconstruction correction methods (attenuation, scatter) and collimator types **(LMEGP, LEHR)** with a SPECT Monte Carlo simulation method for the first time.

In case of an **SLN** in a close proximity to the injection site, attenuation correction alone of SPECT/CT imaging might yield the best **SLN** contrast and scatter correction alone might yield the worst **SLN** contrast. For the same case using an **LMEGP** collimator with less septal penetration characteristics similar **SLN** contrast levels can be achieved against **LEHR** collimator.

The study method validated in this study will enable further Monte Carlo simulations concerning **SLN SPECT** imaging in breast cancer examinations with different gamma camera(s), collimator settings and reconstruction correction methods, and patient variability.

5.1 List of publications produced from the thesis

1. Monte Carlo Simulation of Sentinel Lymph Node SPECT/CT, A. Guvenis, A. Yuksel, *Life Science and Medicine, International Congress On Biological And Medical Sciences*, pp. 72, Oct. 31–Nov. 3,2018.

APPENDIX A. SUPPLEMENTARY RESULTS

Sample SPECT simulation reports (Figure A.1, Figure 39A.2), **SLN** contrast measurements of reconstructed simulations (Table A.1-Table A.4), individual and cumulative averages of **SLN** contrasts for reconstructed simulations (Figure A.3-Figure A.6), the comparison graphs of **SLN** contrast of **LMEGP** and **LEHR** collimators with attenuation correction (Figure A.7, Figure A.8) are appended in this section.

Table A.1
SLN Contrast Measurements of Reconstructed Simulations performed using the LMEGP Collimator.

Reconstruction Methods	**Evaluation Parameters**	**Simulation #**				
		1	2	3	4	5
Attenuation Correction	$\bar{s}$	7165	10126	10489	10137	8383
	$\bar{b}$	3414	3686	3500	4077	2538
	Contrast	0.35	0.47	0.50	0.43	0.54
None	$\bar{s}$	4915	4879	5490	4891	4832
	$\bar{b}$	2690	2309	2274	3028	1546
	Contrast	0.29	0.36	0.41	0.24	0.52
Scatter Correction	$\bar{s}$	1223	2275	3901	923	2882
	$\bar{b}$	803	1047	1808	1661	1039
	Contrast	0.21	0.37	0.37	-0.29	0.47
Attenuation+ Scatter Correction	$\bar{s}$	3588	5827	7289	5710	6887
	$\bar{b}$	1638	1892	3094	2115	2014
	Contrast	0.37	0.51	0.40	0.46	0.55

Table A.2
SLN Contrast Measurements of Reconstructed Simulations performed using the LMEGP Collimator (Continued).

Reconstruction Methods	Evaluation Parameters	Simulation #					Cumulative Average
		6	7	8	9	10	
Attenuation Correction	$\bar{s}$	8827	9466	7819	8655	6418	8749±1347
	$\bar{b}$	3536	5778	2986	5436	4353	3930±1021
	Contrast	0.43	0.24	0.45	0.23	0.19	0.38±0.12
None	$\bar{s}$	5145	4891	4973	4892	4898	4981±198
	$\bar{b}$	2568	3992	2090	3598	3034	2713±726
	Contrast	0.33	0.10	0.41	0.15	0.23	0.30±0.13
Scatter Correction	$\bar{s}$	1759	2199	1305	2037	4987	2349±1270
	$\bar{b}$	1641	2882	788	2668	3062	1740±862
	Contrast	0.03	-0.13	0.25	-0.13	0.24	0.14±0.25
Attenuation+ Scatter Correction	$\bar{s}$	4517	5418	1990	6018	6497	5374±1610
	$\bar{b}$	2465	4648	1300	4238	4682	2809±1280
	Contrast	0.29	0.08	0.21	0.17	0.16	0.32±0.16

Table A.3
SLN Contrast Measurements of Reconstructed Simulations performed using the LEHR Collimator.

Reconstruction Methods	Evaluation Parameters	Simulation #				
		1	2	3	4	5
Attenuation Correction	$\bar{s}$	35057	2695	14893	12448	3567
	$\bar{b}$	9096	1485	4181	5607	1698
	Contrast	0.59	0.29	0.56	0.38	0.35
None	$\bar{s}$	21961	1506	9252	7666	1831
	$\bar{b}$	6154	1021	2755	3934	1079
	Contrast	0.56	0.19	0.54	0.32	0.26
Scatter Correction	$\bar{s}$	10924	1137	4083	5257	934
	$\bar{b}$	3203	851	1566	3719	691
	Contrast	0.55	0.14	0.45	0.17	0.15
Attenuation+ Scatter Correction	$\bar{s}$	21300	2321	7063	12544	2137
	$\bar{b}$	7300	1298	2437	5528	1174
	Contrast	0.49	0.28	0.49	0.39	0.29

```
SIMIND Monte Carlo Simulation Program    V6.1
-------------------------------------------------------------------------
-----
  InputFile: simind         Collimator:pb_sb          SourceFile:smap
  OutputFile:simind185      Cover:     al             SourceMap: vox_man
  Phantom(S):h2o            Crystal:   nai            DensityMap:vox_man
  Phantom(B):bone           BackScatt: lucite         ScoreFile: scattwin
-------------------------------------------------------------------------
-----
  PhotonEnergy              140.00  sy-me    PhotonsPerProj
8080
  SourceType           ZubalVoxman  SPECT    Activity
370.000
  PhantomType          ZubalVoxman  BScatt   DetectorLenght
22.250
  DetectorWidth             29.550  Random   DetectorHeight
0.950
  UpperEneWindowTresh      150.500  Phantom  Distance to det
26.500
  LowerEneWindowTresh      129.500  Resolut  ShiftSource (X)
0.000
  PixelSize  (I)             0.400  Forced   ShiftSource (Y)
0.000
  PixelSize  (J)             0.400  SaveMAP  ShiftSource (Z)
0.000
  HalfLength (S)            48.600           HalfLength  (P)
48.600
  HalfWidth  (S)             0.000           HalfWidth   (P)
0.000
  HalfHeight (S)             0.000           HalfHeigh   (P)
0.000
  EnergyResolution           9.900           MaxScatterOrder
10
-------------------------------------------------------------------------
-----
  GENERAL DATA
  keV/channel                1.000           Compiler          INTEL
Windows
  Photons/Bq                 0.891           StartingAngle
0.000
  CameraOffset (X)           0.000           CoverThickness
0.000
  CameraOffset (Y)           0.000           BackscatterThickn
5.000
  MatrixSize (I)               128           IntrinsicResolut
0.380
  MatrixSize (J)               128           AcceptanceAngle
4.320
  Emission type              2.000           Initial Weight
0.40801E+05
  "NN" Scaling factor        1.000           Energy Channels
512
  Photon Exit phantom            1           CutoffEnergy
92.000
```

```
Random number generator: ranMar
-------------------------------------------------------------------------
-----
  SPECT DATA
  RotationMode            -360.000          Nr of projection
120
  RotationAngle              3.000          Projection start
1
  Orbital fraction           1.000          Projection end
120
-------------------------------------------------------------------------
-----
  COLLIMATOR DATA FOR ROUTINE:Ray-Tracing by MC
  CollimatorCode           sy-me            CollimatorType
Parallel
  HoleSize (X)               0.250          Distance (X)
0.060
  HoleSize (Y)               0.289          Distance (Y)
0.196
  CenterShift (X)            0.155          Collimator effic
0.038
  CenterShift (Y)            0.268          CollimThickness
3.700
  Hole Shape              Hexagonal         Space Coll2Det
0.000
  X-Ray flag                    0
  CollDepValue   (57)        0.000          CollDepValue(58)
0.000
  CollDepValue   (59)        1.000          CollDepValue(60)
0.000
-------------------------------------------------------------------------
-----
  NON-HOMOGENEOUS PHANTOM DATA
  RotationCentre             65, 65         Bone definition
1.190
  CT-Pixel size              0.400          Slice thickness
0.400
  StartImage                    1           No of CT-Images
243
  StepSize                   0.200          CTmapOrientation
0
  MatrixSize   (I)             128          MatrixSize   (J)
128
  CenterPoint  (I)           65.000         CenterPoint  (J)
65.000
  CenterPoint  (K)          122.500         ShiftPhantom (X)
0.000
  ShiftPhantom (Y)           0.000          ShiftPhantom (Z)
0.000
-------------------------------------------------------------------------
-----
  PHANTOM DATA FROM FILE: simind.zub SECTION: 1
```

lymph nodes	1.030	0	0.000E+00	0.000E+00	0.000E+00
0.0					
thyroid	1.050	0	0.000E+00	0.000E+00	0.000E+00
0.0					
trachea	1.000	0	0.000E+00	0.000E+00	0.000E+00
0.0					
cartilage	1.100	0	0.000E+00	0.000E+00	0.000E+00
0.0					
spleen	1.060	0	0.000E+00	0.000E+00	0.000E+00
0.0					
urine	1.030	0	0.000E+00	0.000E+00	0.000E+00
0.0					
feces	1.010	0	0.000E+00	0.000E+00	0.000E+00
0.0					
testes	1.040	0	0.000E+00	0.000E+00	0.000E+00
0.0					
prostate	1.045	0	0.000E+00	0.000E+00	0.000E+00
0.0					
rectum	1.030	0	0.000E+00	0.000E+00	0.000E+00
0.0					
diaphragm	1.030	0	0.000E+00	0.000E+00	0.000E+00
0.0					
bladder	1.040	0	0.000E+00	0.000E+00	0.000E+00
0.0					
lesion	1.060	0	0.000E+00	0.000E+00	0.000E+00
0.0					
dens of axis	1.180	0	0.000E+00	0.000E+00	0.000E+00
0.0					
jaw bone	1.680	0	0.000E+00	0.000E+00	0.000E+00
0.0					
lacrimal glands	1.045	0	0.000E+00	0.000E+00	0.000E+00
0.0					
spinal canal	1.038	0	0.000E+00	0.000E+00	0.000E+00
0.0					
hard palate	1.680	0	0.000E+00	0.000E+00	0.000E+00
0.0					
cerebellum	1.040	0	0.000E+00	0.000E+00	0.000E+00
0.0					
tongue	1.000	0	0.000E+00	0.000E+00	0.000E+00
0.0					
medulla oblongo	1.420	0	0.000E+00	0.000E+00	0.000E+00
0.0					
pons	1.000	0	0.000E+00	0.000E+00	0.000E+00
0.0					
uncus(ear bones	1.180	0	0.000E+00	0.000E+00	0.000E+00
0.0					
sinuses	1.000	0	0.000E+00	0.000E+00	0.000E+00
0.0					
optic nerve	1.070	0	0.000E+00	0.000E+00	0.000E+00
0.0					
cerebral falx	1.040	0	0.000E+00	0.000E+00	0.000E+00
0.0					
eye	1.070	0	0.000E+00	0.000E+00	0.000E+00
0.0					

ORGAN	DENSITY	PIXELS	VOLUME(CC)	MBQ	MBQ/CC	VALUE
skin	1.090	0	0.000E+00	0.000E+00	0.000E+00	0.0
brain	1.040	0	0.000E+00	0.000E+00	0.000E+00	0.0
spinal cord	1.038	0	0.000E+00	0.000E+00	0.000E+00	0.0
skull	1.610	0	0.000E+00	0.000E+00	0.000E+00	0.0
spine	1.330	0	0.000E+00	0.000E+00	0.000E+00	0.0
rib cage & ster	1.410	0	0.000E+00	0.000E+00	0.000E+00	0.0
pelvis	1.290	0	0.000E+00	0.000E+00	0.000E+00	0.0
long bones	1.330	0	0.000E+00	0.000E+00	0.000E+00	0.0
skeletal muscle	1.050	0	0.000E+00	0.000E+00	0.000E+00	0.0
lungs	0.260	0	0.000E+00	0.000E+00	0.000E+00	0.0
heart	1.060	0	0.000E+00	0.000E+00	0.000E+00	0.0
liver	1.060	0	0.000E+00	0.000E+00	0.000E+00	0.0
gall bladder	1.026	0	0.000E+00	0.000E+00	0.000E+00	0.0
kidney	1.050	0	0.000E+00	0.000E+00	0.000E+00	0.0
pharynx	1.000	0	0.000E+00	0.000E+00	0.000E+00	0.0
esophagus	1.030	0	0.000E+00	0.000E+00	0.000E+00	0.0
stomach	1.030	0	0.000E+00	0.000E+00	0.000E+00	0.0
small bowel	1.030	0	0.000E+00	0.000E+00	0.000E+00	0.0
colon	1.030	0	0.000E+00	0.000E+00	0.000E+00	0.0
pancreas	1.040	0	0.000E+00	0.000E+00	0.000E+00	0.0
adrenals	1.025	0	0.000E+00	0.000E+00	0.000E+00	0.0
fat	0.950	0	0.000E+00	0.000E+00	0.000E+00	0.0
blood pool	1.060	0	0.000E+00	0.000E+00	0.000E+00	0.0
gas (bowel)	0.260	0	0.000E+00	0.000E+00	0.000E+00	0.0
fluid (bowel)	1.007	0	0.000E+00	0.000E+00	0.000E+00	0.0
bone marrow	1.030	0	0.000E+00	0.000E+00	0.000E+00	0.0

```
  lens              1.070         0   0.000E+00   0.000E+00   0.000E+00
0.0
  cerebral aquadu   1.040         0   0.000E+00   0.000E+00   0.000E+00
0.0
  teeth             1.920         0   0.000E+00   0.000E+00   0.000E+00
0.0
  TUMORS ADDED FROM FILE:simind.inp
  TUMOR  VOL(pix)     VOL(cc)     MBq        MBq/cc   CHANGE g/cm3
    1       32      0.205E+01   0.366E+03   0.179E+03   none
    2        8      0.512E+00   0.366E+01   0.716E+01   none
-------------------------------------------------------------------------
-----
  SCATTWIN RESULTS USING WINDOW FILE: simind.win

  Win  WinAdded  Range(keV)    ScaleFactor
   1       0    129.5 - 150.5    1.00
   2       1     92.0 - 129.4    1.00

  Win    Total    Scatter   Primary  S/P-Ratio S/T Ratio  Cps/MBq
   1   0.404E+07 0.340E+06 0.370E+07 0.919E-01 0.842E-01 0.911E+02
   2   0.190E+07 0.169E+07 0.203E+06 0.835E+01 0.893E+00 0.427E+02

  Win  Geo(Air)  Pen(Air)  Sca(Air)  Geo(Tot)  Pen(Tot)  Sca(Tot)
   1    95.93%     2.99%     1.08%    96.01%     2.94%     1.05%
   2    94.55%     3.49%     1.96%    97.10%     1.87%     1.03%


  Win   SC 1  SC 2  SC 3  SC 4  SC 5  SC 6  SC 7  SC 8  SC 9  SC10
   1   87.5% 10.8%  1.5%  0.1%  0.0%  0.0%  0.0%  0.0%  0.0%  0.0%
   2   59.6% 26.9%  9.6%  2.9%  0.8%  0.2%  0.0%  0.0%  0.0%  0.0%
-------------------------------------------------------------------------
-----
  Simulation start: 2019:03:08 20:23:07
  Simulation stop : 2019:03:08 20:23:54
  Elapsed time 0h 0min and 47sec
-------------------------------------------------------------------------
-----
  INTERACTIONS IN THE CRYSTAL
  Detector hits......:           5214
  Detector hits/sec..:           167.
  Max val in spectra.:     0.2906E+06
  Max val in images..:     0.2288E+04
  Count rate [Total].:     0.6151E+05
  Count rate [Window]:     0.3370E+05
-------------------------------------------------------------------------
-----
  PHOTONS AFTER 1) COLLIMATOR AND 2) WITHIN E-WIN
  Geometric.....: 96.14%  96.01%
  Penetration...:  2.45%   2.94%
  Scatter Collim:  1.41%   1.05%
  X-ray Collim..:  0.00%   0.00%
-------------------------------------------------------------------------
-----
  RESULTS FROM ENERGY SPECTRUM
```

```
Compton area in spectrum:  0.3187E+07    5.91% (1SD)
  Photo   area in spectrum:  0.4044E+07   14.47% (1SD)
  Pileup  area in spectrum:  0.1498E+06   18.14% (1SD)
-------------------------------------------------------------------------------
-----
  SCATTER RESULTS IN ENERGY WINDOW
  Scatter/Primary......:  0.9192E-01   18.67% (1SD)
  Scatter/Total........:  0.8418E-01
  ScatterOrder  1 .....: 87.4965 %
  ScatterOrder  2 .....: 10.8105 %
  ScatterOrder  3 .....:  1.5326 %
  ScatterOrder  4 .....:  0.1316 %
  ScatterOrder  5 .....:  0.0288 %
-------------------------------------------------------------------------------
-----
  CALCULATED DETECTOR PARAMETERS
  Efficiency [Peak]....:      0.5216     14.47% (1SD)
  Efficiency [Detector]:      0.9520
  Sensitivity [cps/MBq]:     91.0740
  Sensitivity [cpm/uCi]:    202.1842
  Peak/Compton [Peak]..:     53.8347
  Peak/Compton [Area]..:      1.2686
  Peak/Total...........:      0.5479

  Inifile: simind.ini
  Comment: EMISSION VMAN
-------------------------------------------------------------------------------
-----
  Command: simind simind185/in:x22,5x/if:2
```

Figure A.1 Report of simind185 Simulation performed using the LMEGP Collimator.

Table A.4
SLN Contrast Measurements of Reconstructed Simulations performed using the LEHR Collimator (Continued).

Reconstruction Methods	**Evaluation Parameters**	**Simulation #**					**Cumulative Average**
		6	7	8	9	10	
Attenuation Correction	$\bar{s}$	14235	5375	2372	18493	25426	13456±10753
	$\bar{b}$	8512	3079	1244	7857	6700	4946±3023
	Contrast	0.25	0.27	0.31	0.40	0.58	0.40±0.13
None	$\bar{s}$	8086	3149	1517	10036	13535	7854±6472
	$\bar{b}$	5674	2068	884	5303	4398	3327±2032
	Contrast	0.18	0.21	0.26	0.31	0.51	0.33±0.15
Scatter Correction	$\bar{s}$	7034	480	583	7319	9745	4750±3927
	$\bar{b}$	5672	1717	748	4115	3179	2546±1688
	Contrast	0.11	-0.56	-0.12	0.28	0.51	0.17±0.33
Attenuation+ Scatter Correction	$\bar{s}$	10728	811	1548	15526	20136	9411±7816
	$\bar{b}$	7852	2365	1129	6232	5528	4084±2666
	Contrast	0.15	-0.49	0.16	0.43	0.57	0.28±0.30

```
SIMIND Monte Carlo Simulation Program    V6.1
-------------------------------------------------------------------------
-----
  InputFile: simind         Collimator:pb_sb          SourceFile:smap
  OutputFile:simind197      Cover:     al             SourceMap: vox_man
  Phantom(S):h2o            Crystal:   nai            DensityMap:vox_man
  Phantom(B):bone           BackScatt: lucite         ScoreFile: scattwin
-------------------------------------------------------------------------
-----
  PhotonEnergy              140.00  sy-lehr  PhotonsPerProj
8080
  SourceType           ZubalVoxman  SPECT    Activity
370.000
  PhantomType          ZubalVoxman  BScatt   DetectorLenght
22.250
  DetectorWidth             29.550  Random   DetectorHeight
0.950
  UpperEneWindowTresh      150.500  Phantom  Distance to det
26.500
  LowerEneWindowTresh      129.500  Resolut  ShiftSource (X)
0.000
  PixelSize  (I)             0.400  Forced   ShiftSource (Y)
0.000
  PixelSize  (J)             0.400  SaveMAP  ShiftSource (Z)
0.000
  HalfLength (S)            48.600           HalfLength  (P)
48.600
  HalfWidth  (S)             0.000           HalfWidth   (P)
0.000
  HalfHeight (S)             0.000           HalfHeigh   (P)
0.000
  EnergyResolution           9.900           MaxScatterOrder
10
-------------------------------------------------------------------------
-----
  GENERAL DATA
  keV/channel                1.000           Compiler          INTEL
Windows
  Photons/Bq                 0.891           StartingAngle
0.000
  CameraOffset (X)           0.000           CoverThickness
0.000
  CameraOffset (Y)           0.000           BackscatterThickn
5.000
  MatrixSize (I)               128           IntrinsicResolut
0.380
  MatrixSize (J)               128           AcceptanceAngle
2.954
  Emission type              2.000           Initial Weight
0.40801E+05
```

```
"NN" Scaling factor        1.000           Energy Channels
512
  Photon Exit phantom            1           CutoffEnergy
92.000

  Random number generator: ranMar
-------------------------------------------------------------------------
-----
  SPECT DATA
  RotationMode            -360.000           Nr of projection
120
  RotationAngle              3.000           Projection start
1
  Orbital fraction           1.000           Projection end
120
-------------------------------------------------------------------------
-----
  COLLIMATOR DATA FOR ROUTINE:Ray-Tracing by MC
  CollimatorCode           sy-lehr           CollimatorType
Parallel
  HoleSize (X)               0.111           Distance (X)
0.016
  HoleSize (Y)               0.128           Distance (Y)
0.078
  CenterShift (X)            0.064           Collimator effic
0.026
  CenterShift (Y)            0.110           CollimThickness
2.405
  Hole Shape              Hexagonal          Space Coll2Det
0.000
  X-Ray flag                     0
  CollDepValue   (57)        0.000           CollDepValue(58)
0.000
  CollDepValue   (59)        1.000           CollDepValue(60)
0.000
-------------------------------------------------------------------------
-----
  NON-HOMOGENEOUS PHANTOM DATA
  RotationCentre            65, 65           Bone definition
1.190
  CT-Pixel size              0.400           Slice thickness
0.400
  StartImage                     1           No of CT-Images
243
  StepSize                   0.200           CTmapOrientation
0
  MatrixSize   (I)             128           MatrixSize   (J)
128
  CenterPoint  (I)          65.000           CenterPoint  (J)
65.000
  CenterPoint  (K)         122.500           ShiftPhantom (X)
0.000
  ShiftPhantom (Y)           0.000           ShiftPhantom (Z)
0.000
```

PHANTOM DATA FROM FILE: simind.zub SECTION: 1

ORGAN	DENSITY	PIXELS	VOLUME(CC)	MBQ	MBQ/CC	VALUE
skin	1.090	0	0.000E+00	0.000E+00	0.000E+00	0.0
brain	1.040	0	0.000E+00	0.000E+00	0.000E+00	0.0
spinal cord	1.038	0	0.000E+00	0.000E+00	0.000E+00	0.0
skull	1.610	0	0.000E+00	0.000E+00	0.000E+00	0.0
spine	1.330	0	0.000E+00	0.000E+00	0.000E+00	0.0
rib cage & ster	1.410	0	0.000E+00	0.000E+00	0.000E+00	0.0
pelvis	1.290	0	0.000E+00	0.000E+00	0.000E+00	0.0
long bones	1.330	0	0.000E+00	0.000E+00	0.000E+00	0.0
skeletal muscle	1.050	0	0.000E+00	0.000E+00	0.000E+00	0.0
lungs	0.260	0	0.000E+00	0.000E+00	0.000E+00	0.0
heart	1.060	0	0.000E+00	0.000E+00	0.000E+00	0.0
liver	1.060	0	0.000E+00	0.000E+00	0.000E+00	0.0
gall bladder	1.026	0	0.000E+00	0.000E+00	0.000E+00	0.0
kidney	1.050	0	0.000E+00	0.000E+00	0.000E+00	0.0
pharynx	1.000	0	0.000E+00	0.000E+00	0.000E+00	0.0
esophagus	1.030	0	0.000E+00	0.000E+00	0.000E+00	0.0
stomach	1.030	0	0.000E+00	0.000E+00	0.000E+00	0.0
small bowel	1.030	0	0.000E+00	0.000E+00	0.000E+00	0.0
colon	1.030	0	0.000E+00	0.000E+00	0.000E+00	0.0
pancreas	1.040	0	0.000E+00	0.000E+00	0.000E+00	0.0
adrenals	1.025	0	0.000E+00	0.000E+00	0.000E+00	0.0
fat	0.950	0	0.000E+00	0.000E+00	0.000E+00	0.0
blood pool	1.060	0	0.000E+00	0.000E+00	0.000E+00	0.0
gas (bowel)	0.260	0	0.000E+00	0.000E+00	0.000E+00	0.0

```
fluid (bowel)      1.007          0   0.000E+00   0.000E+00   0.000E+00
0.0
  bone marrow        1.030          0   0.000E+00   0.000E+00   0.000E+00
0.0
  lymph nodes        1.030          0   0.000E+00   0.000E+00   0.000E+00
0.0
  thyroid            1.050          0   0.000E+00   0.000E+00   0.000E+00
0.0
  trachea            1.000          0   0.000E+00   0.000E+00   0.000E+00
0.0
  cartilage          1.100          0   0.000E+00   0.000E+00   0.000E+00
0.0
  spleen             1.060          0   0.000E+00   0.000E+00   0.000E+00
0.0
  urine              1.030          0   0.000E+00   0.000E+00   0.000E+00
0.0
  feces              1.010          0   0.000E+00   0.000E+00   0.000E+00
0.0
  testes             1.040          0   0.000E+00   0.000E+00   0.000E+00
0.0
  prostate           1.045          0   0.000E+00   0.000E+00   0.000E+00
0.0
  rectum             1.030          0   0.000E+00   0.000E+00   0.000E+00
0.0
  diaphragm          1.030          0   0.000E+00   0.000E+00   0.000E+00
0.0
  bladder            1.040          0   0.000E+00   0.000E+00   0.000E+00
0.0
  lesion             1.060          0   0.000E+00   0.000E+00   0.000E+00
0.0
  dens of axis       1.180          0   0.000E+00   0.000E+00   0.000E+00
0.0
  jaw bone           1.680          0   0.000E+00   0.000E+00   0.000E+00
0.0
  lacrimal glands    1.045          0   0.000E+00   0.000E+00   0.000E+00
0.0
  spinal canal       1.038          0   0.000E+00   0.000E+00   0.000E+00
0.0
  hard palate        1.680          0   0.000E+00   0.000E+00   0.000E+00
0.0
  cerebellum         1.040          0   0.000E+00   0.000E+00   0.000E+00
0.0
  tongue             1.000          0   0.000E+00   0.000E+00   0.000E+00
0.0
  medulla oblongo    1.420          0   0.000E+00   0.000E+00   0.000E+00
0.0
  pons               1.000          0   0.000E+00   0.000E+00   0.000E+00
0.0
  uncus(ear bones    1.180          0   0.000E+00   0.000E+00   0.000E+00
0.0
  sinuses            1.000          0   0.000E+00   0.000E+00   0.000E+00
0.0
  optic nerve        1.070          0   0.000E+00   0.000E+00   0.000E+00
0.0
```

```
cerebral falx     1.040         0   0.000E+00   0.000E+00   0.000E+00
0.0
  eye               1.070         0   0.000E+00   0.000E+00   0.000E+00
0.0
  lens              1.070         0   0.000E+00   0.000E+00   0.000E+00
0.0
  cerebral aquadu   1.040         0   0.000E+00   0.000E+00   0.000E+00
0.0
  teeth             1.920         0   0.000E+00   0.000E+00   0.000E+00
0.0
  TUMORS ADDED FROM FILE:simind.inp
  TUMOR  VOL(pix)     VOL(cc)     MBq        MBq/cc   CHANGE g/cm3
    1       32      0.205E+01   0.366E+03   0.179E+03   none
    2        8      0.512E+00   0.366E+01   0.716E+01   none
-------------------------------------------------------------------------
-----
  SCATTWIN RESULTS USING WINDOW FILE: simind.win

  Win  WinAdded  Range(keV)    ScaleFactor
   1       0    129.5 - 150.5    1.00
   2       1     92.0 - 129.4    1.00

  Win    Total    Scatter   Primary  S/P-Ratio S/T Ratio  Cps/MBq
   1   0.227E+07 0.189E+06 0.208E+07 0.906E-01 0.831E-01 0.512E+02
   2   0.106E+07 0.942E+06 0.118E+06 0.798E+01 0.889E+00 0.239E+02

  Win  Geo(Air)  Pen(Air)  Sca(Air)  Geo(Tot)  Pen(Tot)  Sca(Tot)
   1    93.90%     4.72%     1.37%    93.93%     4.68%     1.39%
   2    92.03%     4.81%     3.16%    95.88%     2.81%     1.31%


  Win   SC 1  SC 2  SC 3  SC 4  SC 5  SC 6  SC 7  SC 8  SC 9  SC10
   1   87.4% 10.9%  1.5%  0.2%  0.0%  0.0%  0.0%  0.0%  0.0%  0.0%
   2   59.1% 27.2%  9.8%  2.9%  0.8%  0.2%  0.0%  0.0%  0.0%  0.0%
-------------------------------------------------------------------------
-----
  Simulation start: 2019:03:13 22:34:25
  Simulation stop : 2019:03:13 22:34:59
  Elapsed time 0h 0min and 34sec
-------------------------------------------------------------------------
-----
  INTERACTIONS IN THE CRYSTAL
  Detector hits......:           6105
  Detector hits/sec..:           238.
  Max val in spectra.:     0.1650E+06
  Max val in images..:     0.1940E+04
  Count rate [Total].:     0.3452E+05
  Count rate [Window]:     0.1894E+05
-------------------------------------------------------------------------
-----
  PHOTONS AFTER 1) COLLIMATOR AND 2) WITHIN E-WIN
  Geometric.....: 94.48%  93.93%
  Penetration...:  3.82%   4.68%
  Scatter Collim:  1.70%   1.39%
```

```
  X-ray Collim..:  0.00%   0.00%
-------------------------------------------------------------------------
-----
  RESULTS FROM ENERGY SPECTRUM
  Compton area in spectrum:  0.1785E+07    5.91% (1SD)
  Photo   area in spectrum:  0.2273E+07   15.27% (1SD)
  Pileup  area in spectrum:  0.8519E+05   13.72% (1SD)
-------------------------------------------------------------------------
-----
  SCATTER RESULTS IN ENERGY WINDOW
  Scatter/Primary......:  0.9064E-01   15.10% (1SD)
  Scatter/Total........:  0.8310E-01
  ScatterOrder  1 .....: 87.4344 %
  ScatterOrder  2 .....: 10.8894 %
  ScatterOrder  3 .....:  1.4847 %
  ScatterOrder  4 .....:  0.1912 %
  ScatterOrder  5 .....:  0.0003 %
-------------------------------------------------------------------------
-----
  CALCULATED DETECTOR PARAMETERS
  Efficiency [Peak]....:      0.5221     15.27% (1SD)
  Efficiency [Detector]:      0.9517
  Sensitivity [cps/MBq]:     51.1872
  Sensitivity [cpm/uCi]:    113.6355
  Peak/Compton [Peak]..:     66.3845
  Peak/Compton [Area]..:      1.2734
  Peak/Total...........:      0.5486

  Inifile: simind.ini
  Comment: EMISSION VMAN
-------------------------------------------------------------------------
-----
  Command: simind simind197/in:x22,5x/if:2
```

Figure A.2 Report of simind197 Simulation performed using the LEHR Collimator.

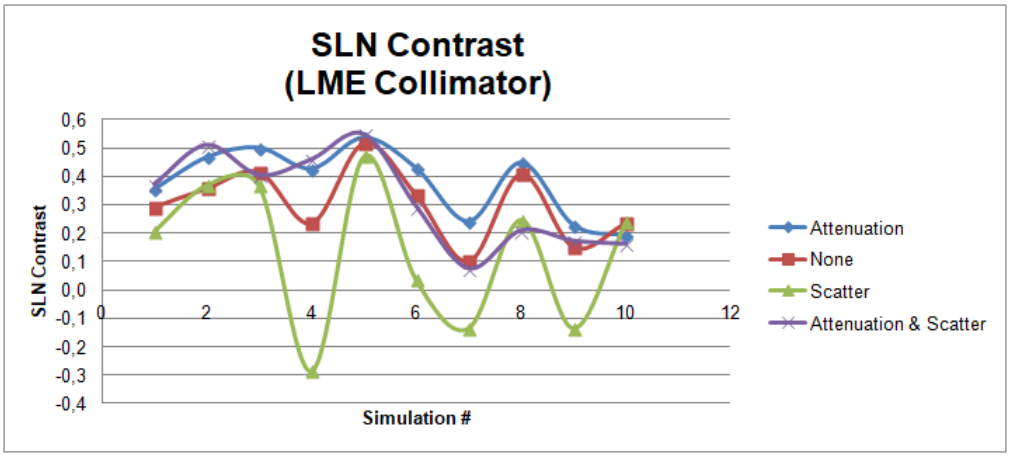

Figure A.3 SLN Contrast Results for Reconstructions of Simulations performed using the LMEGP Collimator.

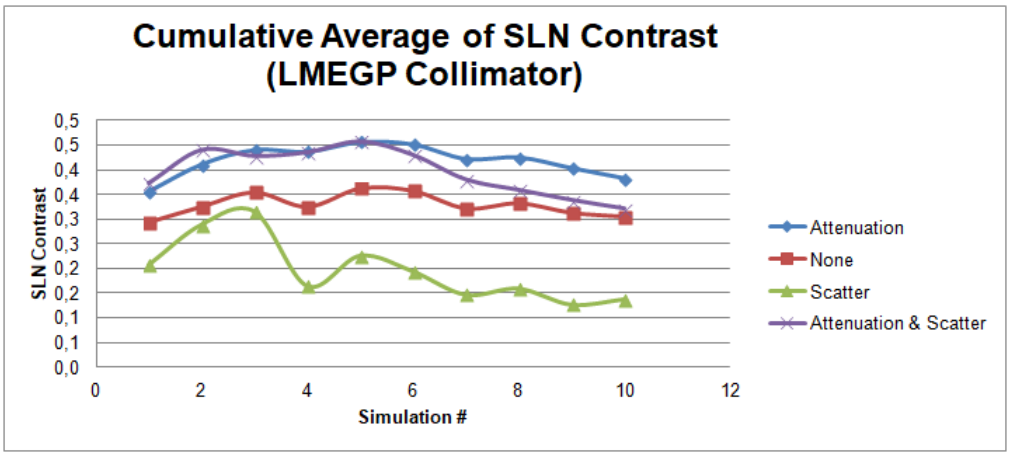

Figure A.4 Cumulative Average of SLN Contrasts for Reconstructions of Simulations performed using the LMEGP Collimator.

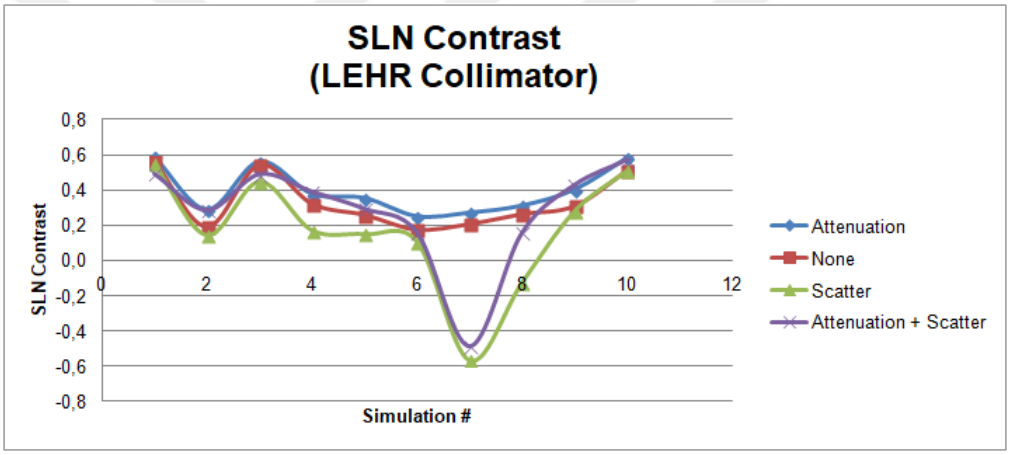

Figure A.5 SLN Contrast Results for Reconstructions of Simulations performed using the LEHR Collimator.

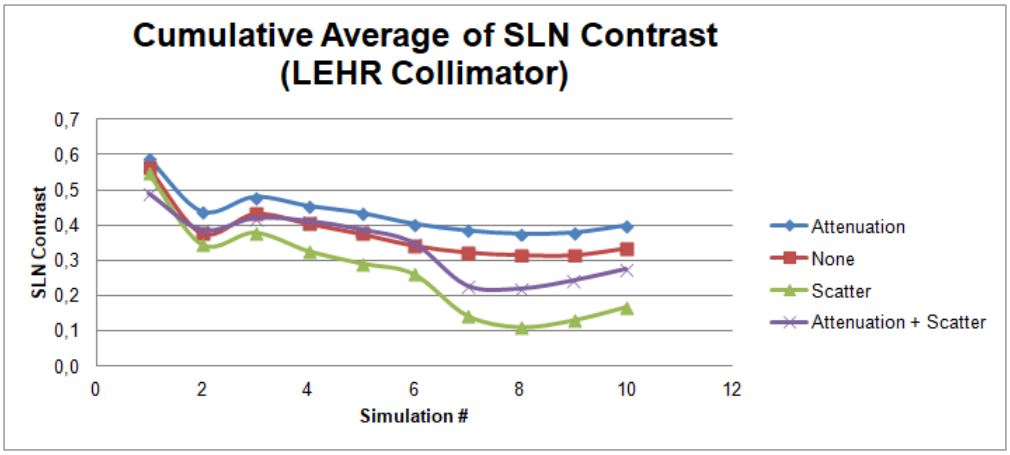

Figure A.6 Cumulative Average of SLN Contrasts for Reconstructions of Simulations performed using the LMEGP Collimator.

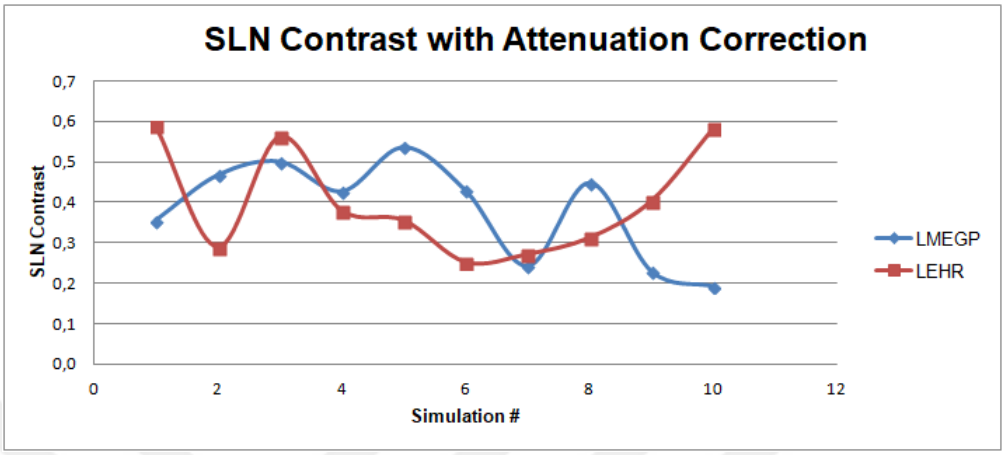

Figure A.7 SLN Contrast of LMEGP and LEHR Collimators with Attenuation Correction.

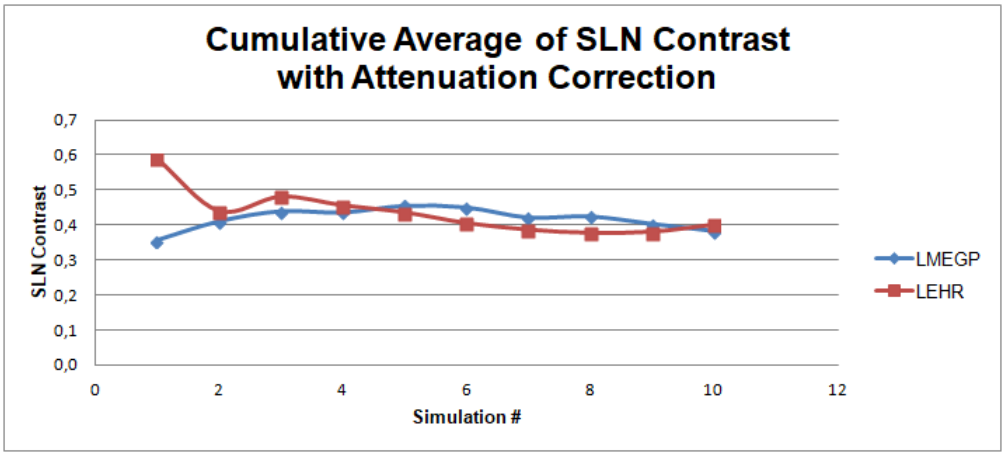

Figure A.8 Cumulative Average of SLN Contrasts for LMEGP and LEHR Collimators with Attenuation Correction.

Table A.5
Penetration and Sensitivity Performance of LMEGP and LEHR Collimators.

Collimator	**Reference File**	**Penetration (%)**	**Sensitivity After Collimator** (cpm/kBq)
LMEGP	simind180.res	2.41	5.55
	simind181.res	2.47	5.46
	simind182.res	2.48	5.46
	simind183.res	2.42	5.45
	simind184.res	2.47	5.44
	simind185.res	2.45	5.46
	simind186.res	2.49	5.45
	simind187.res	2.51	5.46
	simind188.res	2.49	5.42
	simind189.res	2.48	5.47
	LMEGP Average	2.47	5.45
LEHR	simind190.res	3.80	3.08
	simind191.res	3.85	3.07
	simind192.res	3.88	3.07
	simind193.res	3.83	3.06
	simind193.res	3.83	3.06
	simind194.res	3.82	3.07
	simind195.res	3.81	3.07
	simind196.res	3.84	3.06
	simind197.res	3.82	3.07
	simind198.res	3.83	3.07
	simind199.res	3.83	3.08
	LEHR Average	3.43	3.07

REFERENCES

1. Bray, F., J. Ferlay, I. Soerjomataram, R. L. Siegel, L. A. Torre, and A. Jemal, "Global cancer statistics 2018: Globocan estimates of incidence and mortality worldwide for 36 cancers in 185 countries," *CA: A Cancer Journal for Clinicians*, Vol. 68, pp. 394–424, Nov 2018.

2. van der Ploeg, I. M. C., R. A. V. Olmos, B. B. R. Kroon, and O. E. Nieweg, "The hybrid spect/ct as an additional lymphatic mapping tool in patients with breast cancer," *World Journal of Surgery*, Vol. 32, pp. 1930–1934, Sep 2008.

3. van der Ploeg, I. M. C., R. A. V. Olmos, B. B. R. Kroon, E. J. T. Rutgers, and O. E. Nieweg, "The hidden sentinel node and spect/ct in breast cancer patients," *European Journal of Nuclear Medicine and Molecular Imaging*, Vol. 36, pp. 6–11, Jan 2009.

4. Yoneyama, H., H. Tsushima, M. Onoguchi, T. Konishi, K. Nakajima, S. Matsuo, D. Kayano, H. Wakabayashi, A. Inaki, and S. Kinuya, "Optimization of attenuation and scatter corrections in sentinel lymph node scintigraphy using spect/ct systems," *Annals of Nuclear Medicine*, Vol. 29, pp. 248–255, Apr 2015.

5. Moncayo, V. M., J. N. Aarsvold, S. F. Grant, S. C. Bartley, and N. P. Alazraki, "Status of sentinel lymph node for breast cancer," *Seminars in Nuclear Medicine*, Vol. 43, pp. 281–293, Jul 2013.

6. Lerman, H., U. Metser, G. Lievshitz, F. Sperber, S. Shneebaum, and E. Even-Sapir, "Lymphoscintigraphic sentinel node identification in patients with breast cancer: the role of spect-ct," *European Journal of Nuclear Medicine and Molecular Imaging*, Vol. 33, pp. 329–337, Mar 2006.

7. Husarik, D. B., and H. C. Steinert, "Single-photon emission computed tomography/computed tomographyfor sentinel node mapping in breast cancer," *Seminars in Nuclear Medicine*, Vol. 37, pp. 29–33, Jan 2007.

8. Lerman, H., G. Lievshitz, O. Zak, U. Metser, S. Schneebaum, and E. Even-Sapir, "Improved sentinel node identification by spect/ct in overweight patients with breast cancer," *Journal of Nuclear Medicine*, Vol. 48, pp. 201–206, Feb 2007.

9. Uren, R. F., R. Howman-Giles, D. K. Chung, A. J. Spillane, F. Noushi, D. Gillett, L. Gluch, C. Mak, R. West, J. Briody, and H. Carmalt, "Spect/ct scans allow precise anatomical location of sentinel lymph nodes in breast cancer and redefine lymphatic drainage from the breast to the axilla," *The Breast*, Vol. 21, pp. 480–486, Aug 2012.

10. Vercellino, L., J. Ohnona, D. Groheux, A. Slama, P. M. Colletti, S. Chondrogiannis, P. Merlet, M. E. Toubert, and D. Rubello, "Role of spect/ct in sentinel lymph node detection in patients with breast cancer," *Clinical Nuclear Medicine*, Vol. 39, pp. 431–436, May 2014.

11. Mariani, G., L. Moresco, G. Viale, G. Villa, M. Bagnasco, G. Canavese, J. Buscombe, H. W. Strauss, and G. Paganelli, "Radioguided sentinel lymph node biopsy in breast cancer surgery," *Journal of Nuclear Medicine*, Vol. 42, pp. 1198–1215, Aug 2001.

12. Giammarile, F., N. Alazraki, J. N. Aarsvold, R. A. Audisio, E. Glass, S. F. Grant, J. Kunikowska, M. Leidenius, V. Moncayo, R. Uren, and W. J. Oyen, "The eanm and snmmi practice guideline for lymphoscintigraphy and sentinel node localization in breast cancer,"

European Journal of Nuclear Medicine and Molecular Imaging, Vol. 40, pp. 1932–1947, Dec 2013.

13. Krynyckyi, B. R., C. K. Kim, M. R. Goyenechea, P. T. Chan, Z. Y. Zhang, and J. Machac, "Clinical breast lymphoscintigraphy: optimal techniques for performing studies, image atlas, and analysis of images," *Radiographics*, Vol. 24, pp. 121–145, Jan 2004.

14. Lemstra, C., M. Broersma, L. Poot, and P. L. Jager, "Sentinel node detection in patients with breast cancer: low-energy all-purpose collimator or medium-energy collimator?," *Clinical Nuclear Medicine*, Vol. 29, pp. 609–693, Oct 2004.

15. Doshi, N. K., M. Basic, and S. R. Cherry, "Evaluation of the detectability of breast cancer lesions using a modified anthropomorphic phantom," *Breast Cancer*, Vol. 2, p. 10, Nov 1998.

16. Yoneyama, H., H. Tsushima, M. Kobayashi, M. Onoguchi, K. Nakajima, and S. Kinuya, "Improved detection of sentinel lymph nodes in spect/ct images acquired using a low-to medium-energy general-purpose collimator," *Clinical Nuclear Medicine*, Vol. 39, pp. e1–e6, Jan 2014.

17. Brolin, G., K. S. Gleisner, and M. Ljungberg, "Dynamic 99mtc-mag3 renography: images for quality control obtained by combining pharmacokinetic modelling, an anthropomorphic computer phantom and monte carlo simulated scintillation camera imaging," *Physics in Medicine Biology*, Vol. 58, p. 3145, Apr 2013.

18. Zubal, G., G. Gindi, M. Lee, C. Harrell, and E. Smith, "High resolution anthropomorphic phantom for monte carlo analysis of internal radiation sources," in *[1990] Proceedings Third Annual IEEE Symposium on Computer-Based Medical Systems*, pp. 540–547, IEEE, Jun 1990.

19. Ljungberg, M., S.E.Strand, and M. King, eds., *Monte Carlo calculations in nuclear medicine: Applications in diagnostic imaging*, CRC, 2012.

20. Polo, I. O., "Evaluation of the scattered radiation components produced in a gamma camera using monte carlo method," *Revista Brasileira de Engenharia Biomédica*, Vol. 30, pp. 179–188, Jun 2014.

21. Ljungberg, M., S. E. Strand, and M. A. King, "The simind monte carlo program," *Monte Carlo Calculation in Nuclear Medicine: Applications in Diagnostic Imaging*, pp. 145–163, 1998.

22. Zubal, I. G., C. R. Harrell, E. O. Smith, Z. Rattner, G. Gindi, and P. B. Hoffer, "Computerized threeâdimensional segmented human anatomy," *Medical Physics*, Vol. 21, pp. 299–302, Feb 1994.

23. Merlin, T., "Customizable and advanced software for tomographic reconstruction (castor)," 2016.

24. Rasband, W. S., *ImageJ*, Bethesda, Maryland, USA: U. S. National Institutes of Health, 1997-2018. Available: https://imagej.nih.gov/ij/.

25. Dickinson, R. L., W. D. Erwin, D. M. Stevens, L. M. Bidaut, M. V. Mar, H. A. Macapinlac, and R. E. Wendt, "Hybrid modality fusion of planar scintigrams and ct topograms to localize sentinel lymph nodes in breast lymphoscintigraphy: Technical description and phantom studies," *International Journal of Molecular Imaging*, 2011.

26. Dickinson, R. L., W. D. Erwin, D. M. Stevens, L. M. Bidaut, M. V. Mar, H. A. Macapinlac, and R. E. Wendt, "Hybrid modality fusion of planar scintigrams and ct topograms to localize sentinel lymph nodes in breast lymphoscintigraphy: Technical description and phantom studies," *International Journal of Molecular Imaging*, 2011.

27. Ljungberg, M., *The SIMIND Monte Carlo Program Manual.* Available: http://www2.msf.lu.se/simind/download/Simind_manual.pdf.

28. *SIEMENS Symbia T Series System Specifications.* Available: https://3.imimg.com/data3/AC/PC/MY-13438971/gamma-camera.pdf/.

29. Inoue, Y., Y. Abe, K. Kikuchi, K. Matsunaga, R. Masuda, and K. Nishiyama, "Correction of collimator-dependent differences in the heart-to-mediastinum ratio in 123 i-metaiodobenzylguanidine cardiac sympathetic imaging: Determination of conversion equations using point-source imaging," *Journal of Nuclear Cardiology*, Vol. 24, pp. 1725–1736, Oct 2017.

30. Sadrmomtaz, A., and M. N. Asl, "Reliability of scatter correction methods in spect by setting two energy windows," *World Appl Program*, pp. 143–149, 2011.

31. Group, M., *MosaicSuite for ImageJ and Fiji-models, simulation and algorithms for interdisciplinary computing*, 2013. Available: Version lines and rt http://mosaic. mpi-cbg. de.

32. de Nijs, R., V. Lagerburg, T. L. Klausen, and S. Holm, "Improving quantitative dosimetry in 177lu-dotatate spect by energy window-based scatter corrections," *Nuclear Medicine Communications*, Vol. 35, p. 522, May 2014.

33. Jaszczak, R. J., K. L. Greer, J. C. Floyd, C. C. Harris, and R. E. Coleman, "Improved spect quantification using compensation for scattered photons," *Journal of Nuclear Medicine: Official Publication, Society of Nuclear Medicine*, Vol. 25, pp. 893–900, Aug 1984.

34. Ljungberg, M., and S. E. Strand, "Scatter and attenuation correction in spect using density maps and monte carlo simulated scatter functions," *J Nucl Med*, Vol. 31, pp. 1560–1567, Sep 1990.

35. de Nijs, R., V. Lagerburg, T. L. Klausen, and S. Holm, "Improving quantitative dosimetry in 177lu-dotatate spect by energy window-based scatter corrections," *Nuclear Medicine Communications*, Vol. 35, p. 522, May 2014.

36. Kijewski, M. F., "Positron emission tomography (pet) and single-photon emission computed tomography (spect) physics," *Handbook of Neuro-Oncology Neuroimaging*, pp. 353–358, Jan 2016.

37. Mettler, J. F. A., and M. J. Guiberteau, *Essentials of Nuclear Medicine Imaging: Expert Consult-Online and Print*, Elsevier Health Sciences, 2012.

38. Farshid, G., M. Pradhan, J. Kollias, and P. G. Gill, "Computer simulations of lymph node metastasis for optimizing the pathologic examination of sentinel lymph nodes in patients with breast carcinoma," *Cancer*, Vol. 89, pp. 2527–2537, Dec 2000.

39. Alqahtani, M. S., J. E. Lees, S. L. Bugby, L. K. Jambi, and A. C. Perkins, "Lymphoscintigraphic imaging study for quantitative evaluation of a small field of view (sfov) gamma camera," *Journal of Instrumentation*, Vol. 10, pp. 7–11, Jul 2015.

40. Kuehn, T., A. Bembenek, T. Decker, D. L. Munz, M. L. Sautter-Bihl, M. Untch, D. Wallwiener, and C. C. of the German Society of Senology, "A concept for the clinical implementation of sentinel lymph node biopsy in patients with breast carcinoma with special regard to quality assurance," *Cancer*, Vol. 103, pp. 451–461, Feb 2005.

41. Noguchi, A., M. Onoguchi, T. Ohnishi, T. Hashizume, A. Kajita, M. Funauchi, T. Katsuda, and K. Motomura, "Predicting sentinel lymph node metastasis in breast cancer with lymphoscintigraphy," *Annals of Nuclear Medicine*, Vol. 25, pp. 221–222, Apr 2011.

42. Vidal-Sicart, S., O. R. Brouwer, and R. A. Valdé-Olmos, "Evaluation of the sentinel lymph node combining spect/ct with the planar image and its importance for the surgical act," *Revista Espanola de Medicina Nuclear*, Vol. 30, no. 5, pp. 331–337, 2011.

43. Bass, S. S., C. E. Cox, C. J. Salud, G. H. Lyman, C. McCann, E. Dupont, C. Berman, and D. S. Reintgen, "The effects of postinjection massage on the sensitivity of lymphatic mapping in breast cancer," *Journal of the American College of Surgeons*, Vol. 192, pp. 9–16, Jan 2001.

44. Mariani, G., M. Gipponi, L. Moresco, G. Villa, M. Bartolomei, G. Mazzarol, M. C. Bagnara, A. Romanini, F. Cafiero, G. Paganelli, and H. W. Strauss, "Radioguided sentinel lymph node biopsy in malignant cutaneous melanoma," *Journal of Nuclear Medicine*, Vol. 43, pp. 811–827, Jun 2002.

45. Leong, L. K., R. L. Kruger, and M. K. O. MK, "A comparison of the uniformity requirements for spect image reconstruction using fbp and osem techniques," *Journal of Nuclear Medicine Technology*, Vol. 29, pp. 79–83, Jun 2001.

46. King, M., and T. Farncombe, "An overview of attenuation and scatter correction of planar and spect data for dosimetry studies," *Cancer Biotherapy and Radiopharmaceuticals*, Vol. 18, pp. 181–190, Apr 2003.

47. Tsushima, H., T. Takayama, H. Kizu, T. Y. T, Y. Shimonishi, K. Kosakai, M. Murai, and M. Onoguchi, "Advantages of upright position imaging with medium-energy collimator for sentinel node lymphoscintigraphy in breast cancer patients," *Annals of Nuclear Medicine*, Vol. 21, p. 123, Feb 2007.